Evaluating Free Water Elimination for Tractometry in Neonatal Brains

Samantha Kay Eaton

A thesis submitted in partial fulfillment of the requirements for the degree of

Master of Science

University of Washington

2026

Committee:

Ariel Rokem

Scott Murray

Program Authorized to Offer Degree:
Psychology

University of Washington

Abstract

Evaluating Free Water Elimination for Tractometry in Neonatal Brains

Samantha Kay Eaton

Chair of the Supervisory Committee:
Ariel Rokem
Department of Psychology

Diffusion MRI (dMRI) provides a unique non-invasive means of characterizing white matter (WM) organization and structural connectivity during early brain development. However, conventional dMRI pipelines were developed primarily for adult populations and may not adequately account for the distinct tissue composition of the neonatal brain. Incomplete myelination, immature microstructural organization, and reduced tissue packing contribute to elevated free-water content, which can decrease tissue specificity and compromise the reliability of downstream fiber-orientation modeling and tractometry. Free-water elimination (FWE) may address these limitations by separating isotropic free-water signal from anisotropic tissue signal.

This descriptive proof-of-concept study evaluated the effect of FWE on neonatal tractometry using babyFWE, an FWE-based pipeline adapted for neonatal dMRI. BabyFWE was benchmarked against an otherwise matched conventional pipeline in 3 neonates from the Developing Human Connectome Project. Split-half reliability was evaluated for fiber-orientation distribution functions (fODFs), tract delineation, and tract profiles. Voxelwise fODF reliability was quantified using Pearson's r^2 between corresponding split-half fODFs, tract-delineation reliability was assessed using weighted Dice coefficients between tract-density maps, and tract-profile reliability was measured using ICC(2,1) for DKI-FA, DKI-MD, DKI-MK, and DKI-AWF. Tract yield was evaluated separately using whole-brain, non-split tractography.

BabyFWE generally improved reliability relative to conventional processing, although the effect differed among outcome measures. Voxelwise fODF reliability showed modest, spatially heterogeneous improvements, with participant-level mean and median changes averaging 8.0% and 7.3%, respectively. Weighted Dice coefficients increased for all 14 tracts, with an average increase of 71.1% (SD $= 58.7\%$), indicating more consistent tract delineation. Tract yield increased for 7 of the 14 tracts, with no tract showing a negative mean difference. Tract-profile reliability also exhibited modest overall improvements, with variability among tracts and tissue properties.

These findings provide preliminary evidence that FWE can improve multiple dimensions of neonatal tractometry reliability, with particularly consistent benefits for tract delineation and tract yield. Further validation in larger, independent cohorts is needed to establish generalizability and determine whether these reliability improvements also increase the biological and clinical validity of neonatal dMRI measurements.

Acknowledgments

I extend my deepest gratitude to my mentor, Dr. Ariel Rokem, for believing in me as I pivoted from engineering to neuroscience, and for so graciously supporting my academic ambitions. To Dr. Scott Murray, whose kindness was a steady presence, and whose thoughtfulness brought meaning to every interaction. And to Dr. Kelly Chang, whose work laid the foundation for this project, and whose generosity as a scientist was matched by the friendship and reassurance she offered.

Despite the cold, wet Seattle winters, I found an unexpected warmth in the Department of Psychology, the Center for Human Neuroscience, and the Neuroinformatics R&D Group. Their guidance, camaraderie, and laughter softened an intimidating transition and instilled in me a much-needed sense of belonging. I owe special thanks to Catherine Zeigler and McKenzie Hagen for their compassion, which extended beyond the walls of the university and brought light to the year's darkest moments.

And finally, to my mother, Dr. Alesia Eaton, whose faith in me has endured through every season of self-doubt, whose love has sheltered me through every storm, and whose hope has always reminded me that clearer skies lie beyond the horizon. Today, the skies feel brighter.

Dedication

For my grandmother, Katherine, a formidable woman who lived boldly and loved fiercely. She moved through the world with remarkable independence, conviction, and curiosity: a devoted nurse, a champion of women's rights, and an international adventurer.

The beginning of this chapter holds our final embrace, a memory embedded in the path that led me to these very pages. Within the margins of this work lives your love, inseparable from the woman I am becoming, in whom echoes of you endure. As I continue to write my story, I hope the life reflected within its pages makes you proud.

Table of Contents

List of Figures

List of Tables

1 Introduction

1.1 Background

Early life neurodevelopment is characterized by profound structural transformation occurring at rates unmatched throughout the human lifespan, with total brain volume more than doubling within the first year alone (Knickmeyer et al., 2008). During this period, major white matter (WM) pathways, largely established by birth (Gilmore et al., 2018), undergo spatially non-uniform maturation (Matsuzawa et al., 2001). This includes critical microstructural changes such as myelination (Ouyang et al., 2019), which shape lifelong sensorimotor, cognitive, and behavioral function (Lebel and Deoni, 2018).

The need to understand these developmental processes has become increasingly recognized. Recent advances in neuroscience have implicated atypical WM organization in a range of psychiatric and neurological conditions (Forkel et al., 2022), including neurodevelopmental disorders (Zhao et al., 2022). These disorders, which are thought to originate from atypical processes during early brain development (Gilmore et al., 2018; Doi et al., 2022), have become increasingly recognized and diagnosed (Olusanya et al., 2023; Francés et al., 2022). Despite this growing clinical relevance, fundamental gaps remain in our understanding of the brain's organization, connectivity, and developmental trajectories during this critical period.

Exploring infant neural development presents both exceptional challenges and opportunities. Major neuroimaging initiatives have recently begun assembling and releasing large-scale MRI datasets that collectively span the prenatal period through early childhood (Howell et al., 2019; Edwards et al., 2022). These datasets enable investigation of this critical developmental window in a historically understudied population (Nelson et al., 2024). Simultaneously, advances in computational neuroimaging methods now enable *in vivo* investigation of brain structure and connectivity at the scale required for population-level analysis (Bastiani et al., 2019).

Currently, diffusion MRI (dMRI) provides the only available method for non-invasively characterizing WM structural connectivity (Schilling et al., 2019). This technique measures the movement of

water molecules and leverages a fundamental biophysical property: within WM, water diffuses preferentially along axonal fibers, with cellular barriers restricting perpendicular motion (Beaulieu, 2002). These directional constraints produce diffusion patterns that reflect the underlying organization of WM fiber bundles. Computational dMRI pipelines decode these patterns and transform them into quantitative representations of WM organization and structural connectivity (Zhang et al., 2022).

Transforming local diffusion measurements into quantitative models of WM organization involves three primary stages: reconstruction, tractography, and tractometry. During reconstruction, the diffusion signal within each voxel is mathematically transformed into a fiber orientation distribution function (fODF), which estimates the orientations and relative prominence of local fiber bundles (Tournier et al., 2007). Tractography algorithms propagate through these voxel-wise orientation estimates to generate streamlines representing candidate WM trajectories (Jeurissen et al., 2019), which are subsequently delineated into anatomically defined pathways (Yeatman et al., 2012). Tractometry quantifies microstructural tissue properties along each delineated pathway, enabling characterization of regional variation within individual tracts (Kruper et al., 2021). These biologically interpretable tract profiles can then serve as inputs for statistical analyses and clinically relevant neurodevelopmental inference (Yeatman et al., 2012; Kruper et al., 2021).

1.2 Scientific Rationale

While these methods provide a powerful framework for quantifying WM organization, their application to infant dMRI presents substantial methodological challenges. Conventional dMRI pipelines, developed and validated primarily in adult populations, struggle to reliably characterize infant WM due to the distinct anatomical and biophysical properties of the developing brain. These properties, including incomplete WM myelination, high brain-water content, and rapidly changing tissue organization, alter tissue contrast and diffusion properties, complicating the separation and interpretation of tissue-specific signals (Dubois et al., 2014; Ouyang et al., 2019).

During infancy, WM undergoing active myelination and cellular maturation contains comparatively fewer structural barriers to diffusion, resulting in less directionally constrained water motion

(Barkovich et al., 2019; Dubois et al., 2014; Ouyang et al., 2019). Consequently, a greater isotropic water contribution may be present in the measured diffusion signal, reducing the relative contribution of directional information arising from WM tissue. Free-water elimination (FWE) addresses this potential source of signal contamination using a two-compartment biophysical model that separates the measured diffusion signal into isotropic free-water and anisotropic tissue compartments (Pasternak et al., 2009). By explicitly modeling the isotropic free-water contribution, FWE provides a more tissue-specific estimate that may improve the reliability of downstream fiber-orientation modeling and tract-based analyses.

Recently, an FWE-based tractometry framework improved reliability in fiber-orientation estimation, tract delineation, and tract-profile measurements in an aging population in which increased WM free water can compromise diffusion measurements (Chang et al., 2025). However, the biological basis of elevated free water differs between these populations: in aging and neurodegeneration, it may reflect tissue loss and other pathological changes, whereas in infancy, it reflects immature tissue composition, active myelination, and ongoing tissue development (Gullett et al., 2020; Dubois et al., 2014; Ouyang et al., 2019). Despite these distinct biological contexts, the isotropic signal contribution presents a shared methodological challenge.

1.3 Study Objectives

Motivated by this prior work, the present study evaluated whether an FWE-based neonatal tractometry pipeline, hereafter referred to as babyFWE, improved the reliability of neonatal dMRI analysis. To test this, we adapted the FWE tractometry framework developed by Chang et al. (Chang et al., 2025) for application to neonatal dMRI and benchmarked babyFWE against a conventional pipeline without free-water correction. Analyses were conducted in a cohort of neonates ($n = 3$) from the Developing Human Connectome Project (dHCP), a large, publicly available multimodal neuroimaging initiative designed to characterize early human brain development (Fitzgibbon et al., 2020; Edwards et al., 2022). This proof-of-concept evaluation provided preliminary evidence supporting the feasibility of applying FWE to neonatal dMRI analysis and motivating further optimization and validation in larger, independent datasets.

2 Methods

2.1 Participants

MRI data from 3 neonates enrolled in the Developing Human Connectome Project (dHCP) were leveraged in this analysis. The dHCP is a multimodal neuroimaging study of fetal, term-born, preterm-born, and at-risk infants spanning approximately 20 to 45 weeks postmenstrual age. The project was established to map typical and atypical patterns of brain structure, function, and connectivity during the perinatal period. The study protocol was approved by the United Kingdom Health Research Authority, and written parental consent was obtained for all participating families (Fitzgibbon et al., 2020; Edwards et al., 2022).

Participants were selected as practical starting candidates for pipeline development and benchmarking based on a combination of recommendations from collaborators with prior experience processing dHCP data using babyAFQ (Grotheer et al., 2022, 2023) and consideration of postmenstrual age. Selection therefore prioritized demonstrated processing feasibility and technical suitability rather than systematic or representative sampling of the full dHCP cohort. Complete subject-level demographic and clinical metadata were not available for the present analysis; participant and session identifiers are provided in Appendix A.

2.2 MRI Acquisition

Imaging was performed at the Evelina Newborn Imaging Centre, Centre for the Developing Brain, King's College London, United Kingdom, using a dedicated neonatal imaging system. Data were acquired on a 3 T Philips Achieva magnetic resonance imaging (MRI) scanner equipped with a dedicated 32-channel neonatal head coil and customized positioning cradle (Hughes et al., 2017). The acquisition protocol was optimized for neonatal brain tissue properties and motion tolerance (Hughes et al., 2017; Cordero-Grande et al., 2018, 2020; Hutter et al., 2018a). Participants were fed, swaddled, and scanned primarily during natural sleep (Edwards et al., 2022). The present analysis leveraged the T1-weighted (T1w) and

T2-weighted (T2w) structural images and multishell diffusion-weighted imaging (DWI) data acquired from each participant.

2.2.1 Diffusion-Weighted Imaging

DWI data were acquired using a neonatal-optimized multishell echo-planar imaging sequence (Tournier et al., 2020). The acquisition comprised 300 volumes, including 20 volumes at $b = 0$ s/mm² and three nonzero diffusion-weighting shells: 64 directions at $b = 400$ s/mm², 88 directions at $b = 1{,}000$ s/mm², and 128 directions at $b = 2{,}600$ s/mm². Measurements within each shell were distributed across anterior-to-posterior, posterior-to-anterior, right-to-left, and left-to-right phase-encoding directions (Hutter et al., 2018b).

Images were acquired with a multiband factor of 4, a SENSE acceleration factor of 1.2, and a partial-Fourier factor of 0.86. The acquired spatial resolution was 1.5 × 1.5 mm² in plane, with a slice thickness of 3 mm and 1.5 mm of overlap between adjacent slices. The TR was 3,800 ms, and the TE was 90 ms (Edwards et al., 2022). Image reconstruction was performed using a dedicated SENSE reconstruction algorithm (Hennel et al., 2016; Zhu et al., 2016; Cordero-Grande et al., 2018).

2.3 Preprocessing

2.3.1 dHCP Preprocessing

Preprocessed multishell DWI data were obtained from the dHCP second data release (Edwards et al., 2022) and processed using the dHCP neonatal FSL EDDY-based diffusion pipeline (Bastiani et al., 2019). The resulting preprocessed DWI, corresponding b-values and b-vectors, and diffusion-space brain mask were used directly in subsequent processing steps.

2.3.2 Resolution Resampling

DWI data were resampled from their native anisotropic resolution ($1.172 \times 1.172 \times 1.5$ mm) to 1.5 mm isotropic resolution using the `reslice` function in DIPY (Garyfallidis et al., 2014). Isotropic voxel dimensions were used to facilitate subsequent tractography (McMaster et al., 2025). Linear interpolation (`order=1`) was applied to the DWI data, whereas nearest-neighbor interpolation (`order=0`) was applied to the corresponding brain mask to preserve discrete mask labels. The resampled mask was thresholded

(> 0.5) to guarantee binary output. The corresponding b-values and b-vectors were retained without modification, as resampling altered only the image grid.

2.4 Reconstruction

2.4.1 Free-Water Elimination

To reduce the contribution of free water to the diffusion signal, a multishell free-water diffusion tensor imaging (FWDTI) model was fitted to the DWI data. The model represents the signal in each voxel as a volume-fraction-weighted mixture of two compartments (Pierpaoli and Jones, 2004): a tissue compartment described by a diffusion tensor, allowing for anisotropic diffusion, and a free-water compartment described by a fixed isotropic diffusivity representing approximately unrestricted water diffusion. This two-compartment model can be expressed as:

$$S(\boldsymbol{\theta}, b) = S_0 \left[(1 - f) \exp\left(-b \boldsymbol{\theta}^T \mathbf{Q} \boldsymbol{\theta} \right) + f \exp\left(-b D_{\text{iso}} \right) \right] \tag{2.1}$$

where $S(\boldsymbol{\theta}, b)$ is the diffusion-weighted signal measured for gradient direction $\boldsymbol{\theta}$ at diffusion weighting b, S_0 is the non-diffusion-weighted signal, $\mathbf{Q}$ is the symmetric tissue diffusion tensor, f is the estimated free-water volume fraction, and D_{iso} is the fixed diffusivity of free water at body temperature, set to 3.0×10^{-3} mm²/s.

The FWDTI model is particularly well suited to multishell diffusion data, as measurements acquired across multiple diffusion-weighting values permit joint estimation of the tissue diffusion tensor and free-water volume fraction using nonlinear least-squares optimization (Hoy et al., 2014). Model parameters were estimated using the FWDTI implementation described by Henriques et al. (2017) via the free-water-elimination (FWE) software developed by Chang et al. (2025).

Once fitted, the model estimated the tissue diffusion tensor ($\mathbf{Q}$) and free-water volume fraction (f), effectively decomposing the measured diffusion signal into tissue and free-water contributions. The estimated free-water contribution was then subtracted from the measured diffusion signal to produce the FWE signal:

$$S_{\text{FWE}}(\boldsymbol{\theta}, b) = S(\boldsymbol{\theta}, b) - S_0 f \exp\left(-b D_{\text{iso}} \right). \tag{2.2}$$

where $S_{\mathrm{FWE}}(\boldsymbol{\theta}, b)$ denotes the resulting free-water-corrected DWI signal. Despite modeling the tissue compartment ($\mathbf{Q}$) as a single diffusion tensor, the free-water correction removes only the isotropic free-water contribution, preserving the directional information in the measured signal. $\mathbf{Q}$ therefore serves only to isolate the free-water fraction rather than to constrain the underlying fiber geometry, so the angular information needed to resolve crossing fiber populations is retained for subsequent reconstruction (Rokem et al., 2015).

2.4.2 Constrained Spherical Deconvolution

A WM response function was estimated from the original, uncorrected diffusion-weighted signal with DIPY's `auto_response_ssst` procedure. Estimation was performed using the lowest nonzero diffusion-weighting shell in the dHCP acquisition ($b = 400$ s/mm^2), a region-of-interest radius of 10 voxels, and a fractional-anisotropy threshold of 0.7. This response function was subsequently used to fit constrained spherical deconvolution (CSD) models to both the original and FWE-corrected diffusion-weighted signals within the participant-specific WM mask, with identical fitting parameters applied across conditions (Tournier et al., 2007; Garyfallidis et al., 2014). The maximum spherical-harmonic order was set to 8, and the resulting fiber-orientation distribution functions (fODFs) were evaluated on DIPY's symmetric362 sphere (Chang et al., 2025).

2.5 Tractography

Tractography was performed using pyAFQ version 2.1.0 (Kruper et al., 2021, 2025). The conventional pipeline used the original dMRI data as input to pyAFQ, whereas the babyFWE pipeline used the corresponding FWE-corrected data. Within pyAFQ, fODFs were internally estimated from all diffusion-weighting shells using constrained spherical deconvolution (CSD) with the manually estimated response function described in Section 2.4.2 (Tournier et al., 2007). Whole-brain tractography used DIPY's local probabilistic tracking algorithm, with streamline direction sampled at each step from the fiber-orientation distribution function (Garyfallidis et al., 2014). Seeding and stopping were governed by an FA threshold of 0.2, with seeds placed within the thresholded mask at a density of two per voxel along each dimension, corresponding to eight seeds per voxel, and streamlines terminated when FA fell

below the threshold. Identical tractography parameters were applied to the conventional and babyFWE pipelines.

2.5.1 Bundle Segmentation

The resulting whole-brain streamlines were segmented into anatomically defined WM pathways using the babyAFQ framework, which adapts pyAFQ's automated fiber quantification methods for the developing brain and defines pathways specific to the neonatal WM (Grotheer et al., 2022, 2023). Each participant was registered to the UNC neonatal template distributed with babyAFQ (`UNCNeo-withCerebellum-for-babyAFQ`), using the mean non-diffusion-weighted (b0) image as the registration image. Bundle-specific inclusion and exclusion regions of interest, defined in template space and back-transformed into each participant's native space, were used to classify candidate streamlines according to babyAFQ's neonatal pathway definitions. Streamlines were then resampled to 100 points, and candidate bundles were refined using pyAFQ's default bundle-cleaning procedure, which iteratively removes streamlines that deviate substantially from a tract's mean trajectory (Yeatman et al., 2012).

The retained pathways included the forceps major and forceps minor, together with the following 12 bilateral pathways: anterior thalamic radiation, arcuate fasciculus, cingulum cingulate, corticospinal tract, inferior fronto-occipital fasciculus, inferior longitudinal fasciculus, middle longitudinal fasciculus, optic radiation, posterior arcuate fasciculus, superior longitudinal fasciculus, uncinate fasciculus, and vertical occipital fasciculus, for 26 pathways in total. The same registration, pathway-definition, and bundle-cleaning procedures were applied to both the conventional and babyFWE pipelines.

2.6 Tractometry

Tractometry was performed using pyAFQ version 2.1.0 (Kruper et al., 2021, 2025).

2.6.1 Tract Profiles

For each delineated pathway, tissue properties were sampled at the 100 nodes established during bundle segmentation, providing anatomically corresponding positions from one tract endpoint to the other. Diffusion metrics at each node were computed as weighted averages across the pathway's constituent

streamlines, with streamlines nearer the tract's central trajectory contributing more heavily than those farther from it (Yeatman et al., 2012; Kruper et al., 2021).

Tissue properties were derived from the diffusion kurtosis imaging (DKI) model (Jensen et al., 2005), using the DIPY software library (Garyfallidis et al., 2014; Henriques et al., 2021). This model captures tissue microstructural complexity by quantifying diffusion features that reflect barriers, restrictions, and heterogeneity within the tissue microenvironment. Derived measures included fractional anisotropy (DKI-FA) and mean diffusivity (DKI-MD), which describe the directionality and magnitude of diffusion, respectively, as well as mean kurtosis (DKI-MK), which quantifies the degree of non-Gaussian diffusion and increases with tissue microstructural complexity. Axonal water fraction (DKI-AWF) was additionally estimated using the biophysically motivated White Matter Tract Integrity (WMTI) model (Fieremans et al., 2011), reflecting the proportion of tissue water residing within axons and providing a measure related to axonal density and WM maturation.

For both the conventional and babyFWE pipelines, tissue properties were estimated from the original, uncorrected diffusion signal to avoid introducing dependence on the FWDTI model fit (Correia et al., 2024; Golub et al., 2021); the FWE-corrected signal was used exclusively for tractography and bundle segmentation, following Chang et al. (2025).

2.7 Analysis

To evaluate whether free-water elimination improves the reliability and yield of infant tractometry, two complementary analyses were conducted. Split-half reliability analysis assessed the reproducibility of pipeline outputs across three stages of processing, while tract-yield analysis evaluated whether free-water elimination increased the rate of successful tract reconstruction. Given the preliminary nature of the study and the small sample size ($n = 3$), the analyses were designed to characterize descriptive patterns rather than test formal statistical hypotheses; accordingly, no inferential statistical tests were performed.

2.7.1 Reliability Analysis

Split-half reliability was evaluated at three stages of the tractometry workflow: fODF reconstruction, tract delineation, and tract-profile estimation. At each stage, reliability was calculated separately for the

conventional and babyFWE pipelines using the two split-half datasets, after which the resulting between-pipeline differences were summarized.

For the tract-based analyses reported below, left- and right-hemisphere values were averaged within each participant, collapsing the 26 WM tracts into 14 categories: 12 bilateral pairs, the forceps major, and the forceps minor.

2.7.1.1 Split-Half Dataset Generation

Within-participant split-half datasets were generated from the resampled multishell diffusion MRI data. Volumes were partitioned evenly within each b-value shell according to acquisition order, with the first half of the volumes assigned to one split and the second half assigned to the other; this chronological partitioning strategy was used in place of random assignment, which produced visually implausible bundle reconstructions in the split-half data for this infant cohort. The resulting splits were non-overlapping and contained equal numbers of measurements: each split included 10 non-diffusion-weighted measurements at $b = 0$ s/mm^2, together with 32, 44, and 64 diffusion-weighted measurements at $b = 400$, 1,000, and 2,600 s/mm^2, respectively. Reconstruction, tractography, tract delineation, and tractometry were then performed independently for each split.

2.7.1.2 Fiber-Orientation Distribution Functions (fODFs)

The voxelwise reliability of fODF reconstruction was quantified within each participant's WM mask. For each pipeline, the two split-half fODF estimates were sampled at 362 directions, and explained variance was calculated as the squared Pearson correlation coefficient (r^2) between the estimates, producing a three-dimensional r^2 map for each participant and pipeline. The effect of babyFWE on fODF reliability was evaluated by calculating the symmetric percent change between the babyFWE and conventional r^2 maps at each WM voxel:

$$\Delta r_v^2\,(\%) = \frac{r^2_{v,\text{babyFWE}} - r^2_{v,\text{conventional}}}{\frac{1}{2}\left(r^2_{v,\text{babyFWE}} + r^2_{v,\text{conventional}}\right)} \times 100. \tag{2.3}$$

where Δr_v^2 denotes the voxelwise symmetric percent difference in explained variance, and $r^2_{v,\text{babyFWE}}$ and $r^2_{v,\text{conventional}}$ denote the voxelwise explained variance for the babyFWE and conventional pipelines,

respectively.

For each participant, the voxelwise symmetric-percent-change map was summarized by its mean and median. For Δr_v^2 and its per-participant mean and median, positive values indicated greater split-half reliability for the babyFWE pipeline, whereas negative values indicated greater reliability for the conventional pipeline.

2.7.1.3 Tract Delineation

The spatial consistency of tract delineation was evaluated using the weighted Dice coefficient (Cousineau et al., 2017). For each pathway, streamline-density maps were generated separately from the two split-half tractograms by counting the number of streamlines passing through each voxel in the resampled diffusion-image space. The weighted Dice coefficient was then calculated as:

$$\text{Weighted Dice} = \frac{2\sum_v \min\left(d_{A,v}, d_{B,v}\right)}{\sum_v d_{A,v} + \sum_v d_{B,v}}. \tag{2.4}$$

where $d_{A,v}$ and $d_{B,v}$ denote the streamline-density values at voxel v in the two split-halves. Values range from 0 to 1, with higher values indicating greater agreement in both the spatial distribution and relative streamline density of the pathway. When a pathway was reconstructed in only one split-half, or was absent from both split-halves, it was omitted from analysis. Symmetric percent change in weighted Dice was then calculated between the conventional and babyFWE pipelines for each participant and pathway as:

$$\%\Delta D = \frac{D_{\text{babyFWE}} - D_{\text{conventional}}}{\frac{1}{2}\left(D_{\text{babyFWE}} + D_{\text{conventional}}\right)} \times 100, \tag{2.5}$$

where positive values indicate greater spatial consistency of tract delineation following babyFWE, and negative values indicate greater consistency for the conventional pipeline.

2.7.1.4 Tissue Profiles

Split-half reliability of the tract profiles was quantified using ICC(2,1), a two-way random-effects, single-measurement, absolute-agreement intraclass correlation coefficient, reported as ICC2 ("Single random raters") by Pingouin (Vallat, 2018). For each participant, pathway, and tissue property, the 100 tract-profile nodes were treated as measurement targets, and the two split-halves were treated as raters. ICCs were cal-

culated separately for DKI-FA, DKI-MD, DKI-MK, and DKI-AWF. When a pathway was present in only one split-half, or was absent from both split-halves, it was omitted from analysis. The raw difference in ICC was then calculated between the conventional and babyFWE pipelines for each participant, pathway, and tissue property as:

$$\Delta\text{ICC} = \text{ICC}_{\text{babyFWE}} - \text{ICC}_{\text{conventional}} \tag{2.6}$$

where positive values indicate higher reliability following babyFWE.

2.7.2 Tract Yield

Tract yield was assessed for each participant using whole-brain, non-split tractography by comparing whether each of the 26 pathways was successfully reconstructed by the conventional and babyFWE pipelines. A pathway was considered successfully reconstructed if it contained at least 10 streamlines (Chang et al., 2025). For each pathway, tract yield was represented as a binary outcome for each pipeline, and the difference between pipelines was calculated as:

$$\Delta\text{Yield} = \text{Yield}_{\text{babyFWE}} - \text{Yield}_{\text{conventional}} \tag{2.7}$$

Values of $+1$, 0, and -1 indicated that a pathway was gained, unchanged, or lost with babyFWE, respectively. For bilateral pathways, the per-hemisphere ΔYield values were averaged across the left and right hemispheres and expressed as a percentage ($\%$), such that 100% indicated a bilateral change (both hemispheres gained or lost the pathway), 50% indicated a unilateral change (one hemisphere only), and 0% indicated no change in either hemisphere.

3 Results

3.1 Split-Half Reliability

Reliability was assessed across split-half datasets to evaluate the effect of babyFWE at each stage of the tractometry pipeline. All reported differences are expressed relative to the conventional pipeline, such that positive values favor babyFWE and negative values favor the conventional pipeline.

3.1.1 Fiber-Orientation Distribution Functions (r^2)

fODF reliability was quantified voxelwise within the WM mask as the explained variance (Pearson's r^2) between the split-half fODFs, each evaluated at 362 points on the sphere. For the representative participant (C2; Table B.1), the voxelwise percent-change map (Fig. 3.1a) exhibited local increases and decreases interspersed throughout the WM mask without an obvious anatomically clustered pattern.

The corresponding voxelwise distribution (Fig. 3.1b) was right-skewed: most voxels exhibited relatively modest changes clustered near 0%, while a smaller subset showed substantially larger reliability gains. Consequently, this participant's mean percent change (9.6%) was nearly twice its median change (5.6%; Table B.1), indicating that the overall improvement was largely driven by relatively few voxels exhibiting large increases in reliability rather than by a uniform shift within the WM mask.

Of the 3 participants, 2 showed higher split-half fODF reliability following babyFWE according to both the mean and median voxelwise summaries (Fig. 3.1c; Table B.1). For the other participant, both summaries indicated lower reliability following babyFWE. Among participants, the average voxelwise mean percent change was 8.0% (SD $= 15.4\%$), while the average voxelwise median percent change was 7.3% (SD $= 10.9\%$).

3.1.2 Tract Delineation (Dice)

Tract delineation reliability was quantified using the weighted Dice coefficient between tract-density maps reconstructed from the split-half datasets. Averaged across tracts, weighted Dice coefficients were higher following babyFWE (0.58, SD $= 0.17$) than for the conventional pipeline (0.38, SD $= 0.24$); tract-specific values are reported in Table C.1.

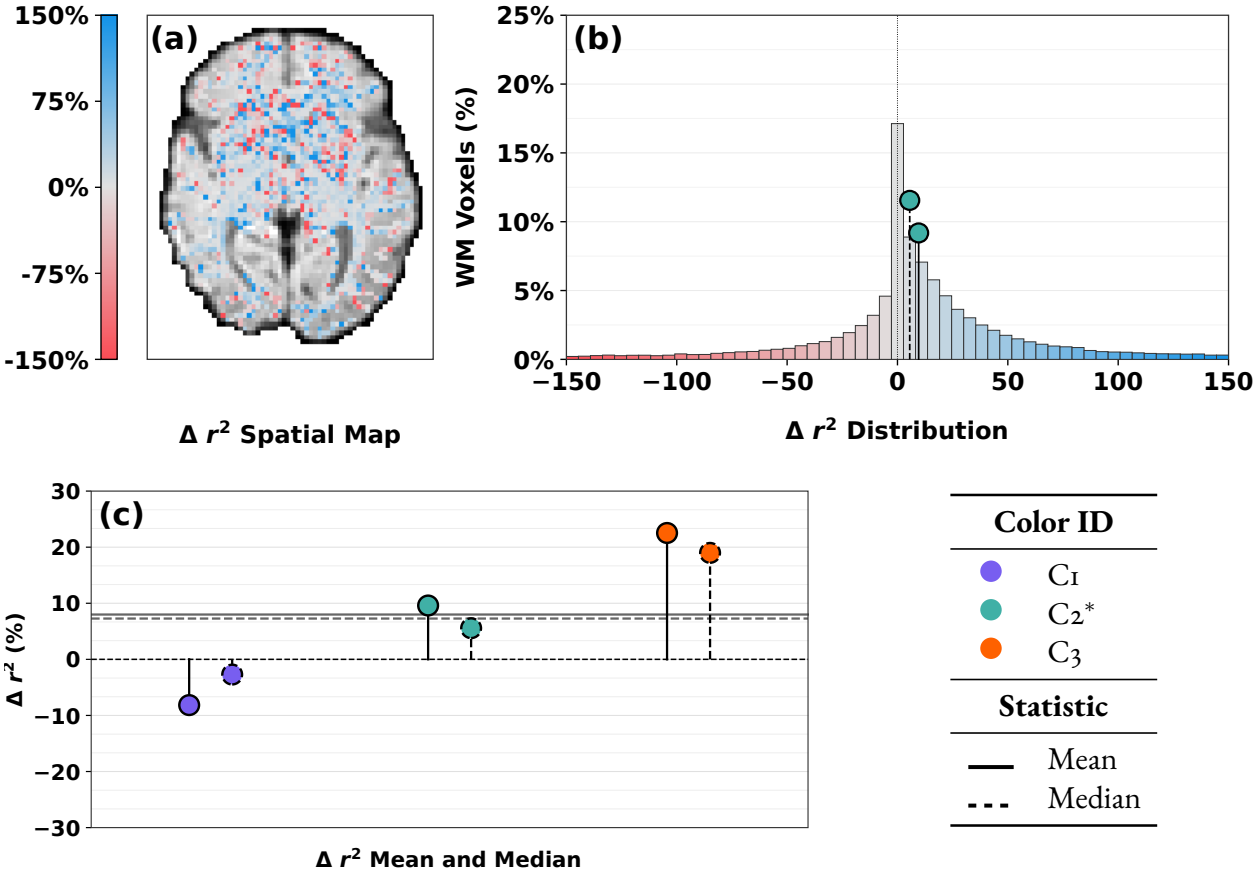

Figure 3.1: Voxelwise and participant-level changes in fODF split-half reliability following babyFWE. **(a)** Spatial map of voxelwise percent change in explained variance (Δr^2) within the WM mask for representative participant C2*; blue/red indicate higher/lower reliability, respectively, following babyFWE. **(b)** Corresponding voxelwise distribution, colored on the same scale as (a); teal markers show this participant's mean and median. **(c)** Mean (solid) and median (dashed) Δr^2 per participant, with participant colors and line styles defined in the adjacent key.

Weighted Dice coefficients increased for 13 of 14 tracts following babyFWE; the remaining tract could not be evaluated because it was not reconstructed by the conventional pipeline (Fig. 3.2). The magnitude of improvement varied substantially across tracts, ranging from 10.5% for the optic radiation to 200.0% for the vertical occipital fasciculus. Large improvements were also observed for the uncinate (152.0%) and posterior arcuate (140.1%). Averaged across tracts, babyFWE increased the weighted Dice coefficient by 71.1% (SD = 58.7%).

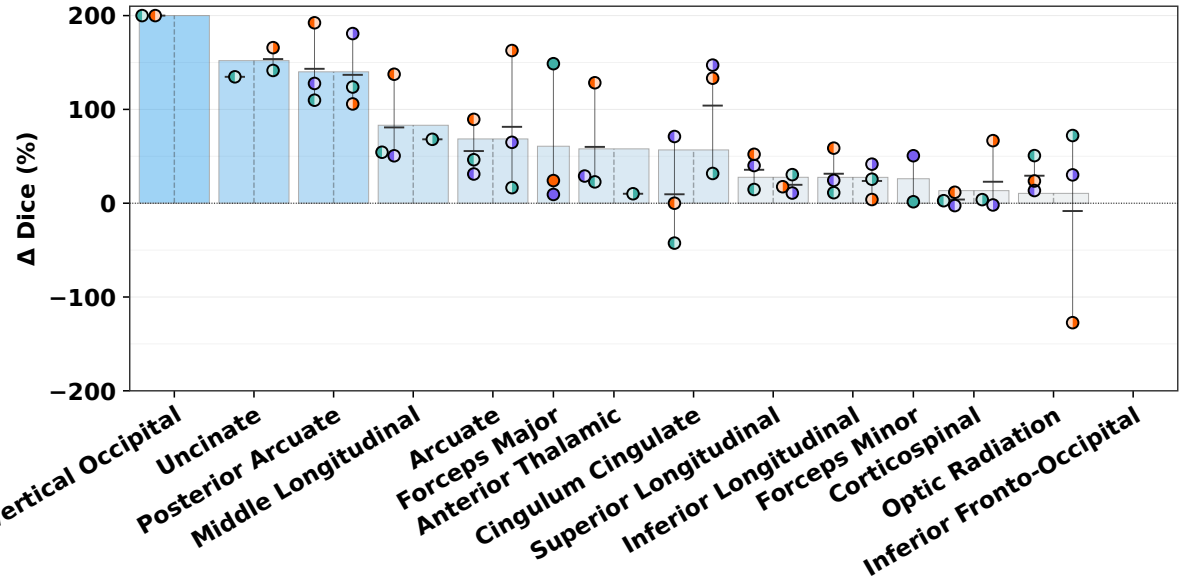

Figure 3.2: Change in weighted Dice coefficient following babyFWE. Bars represent the mean percent change for each tract, with points indicating participant-level values. For bilateral tracts, bar halves and semicircle markers represent left- and right-hemisphere values, while bar height represents the bilateral average. Unilateral tracts are represented by solid bars and filled-circle markers.

3.1.3 Tract Profiles (ICC)

Tract-profile reliability was assessed using ICC(2,1) between corresponding profiles reconstructed from the split-half datasets. ICCs were calculated separately for DKI-FA, DKI-MD, DKI-MK, and DKI-AWF. The effect of babyFWE was quantified as the raw ICC difference (FWE − DWI) for each participant and tract (Fig. 3.3a–d).

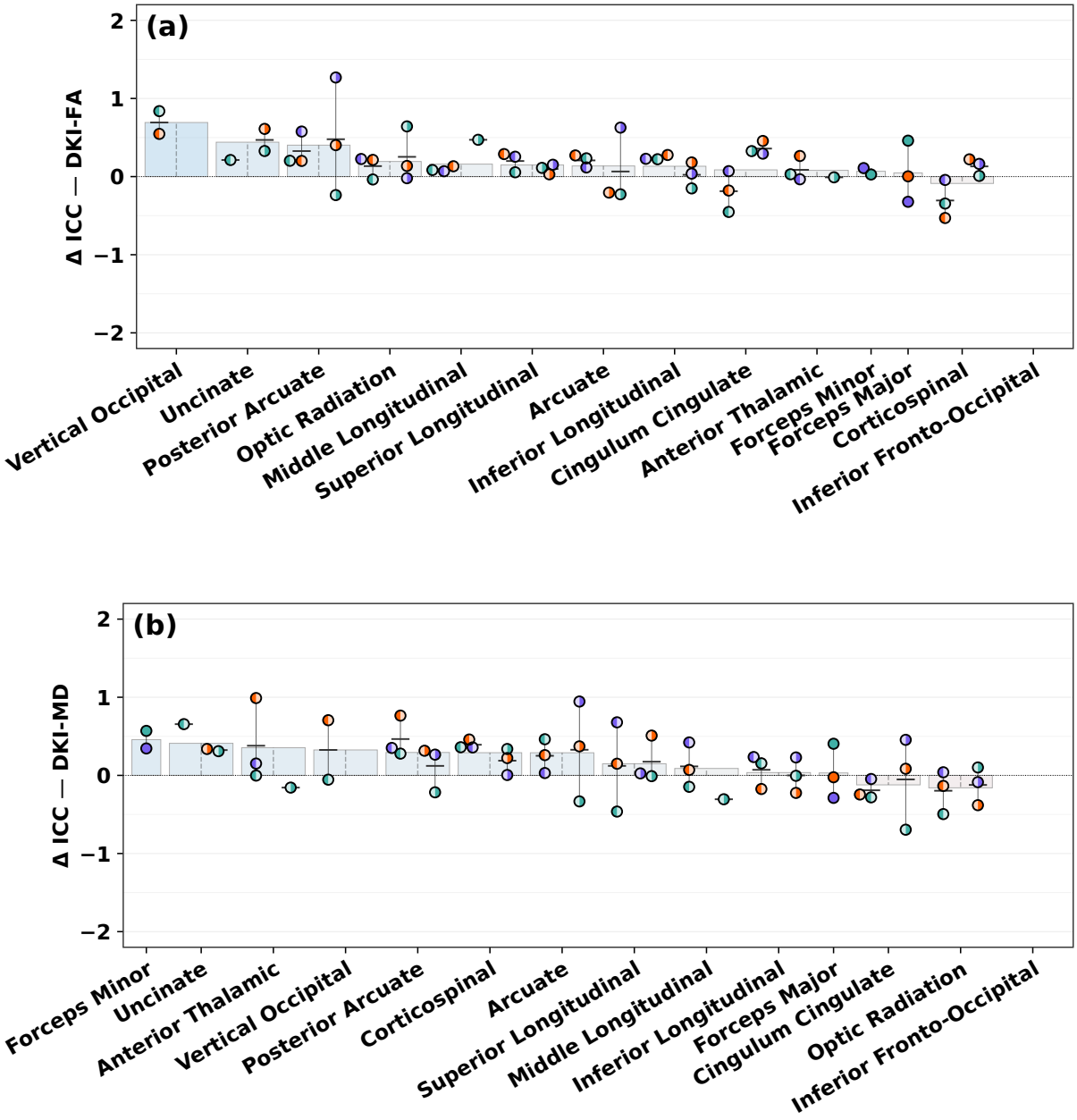

Figure 3.3: Change in tract-profile reliability following babyFWE: **(a)** DKI-FA, **(b)** DKI-MD, **(c)** DKI-MK, and **(d)** DKI-AWF. Bars represent the mean raw ICC difference for each tract, with points indicating participant-level values. For bilateral tracts, bar halves and semicircle markers represent left- and right-hemisphere values, while bar height represents the bilateral average. Unilateral tracts are represented by solid bars and filled-circle markers.

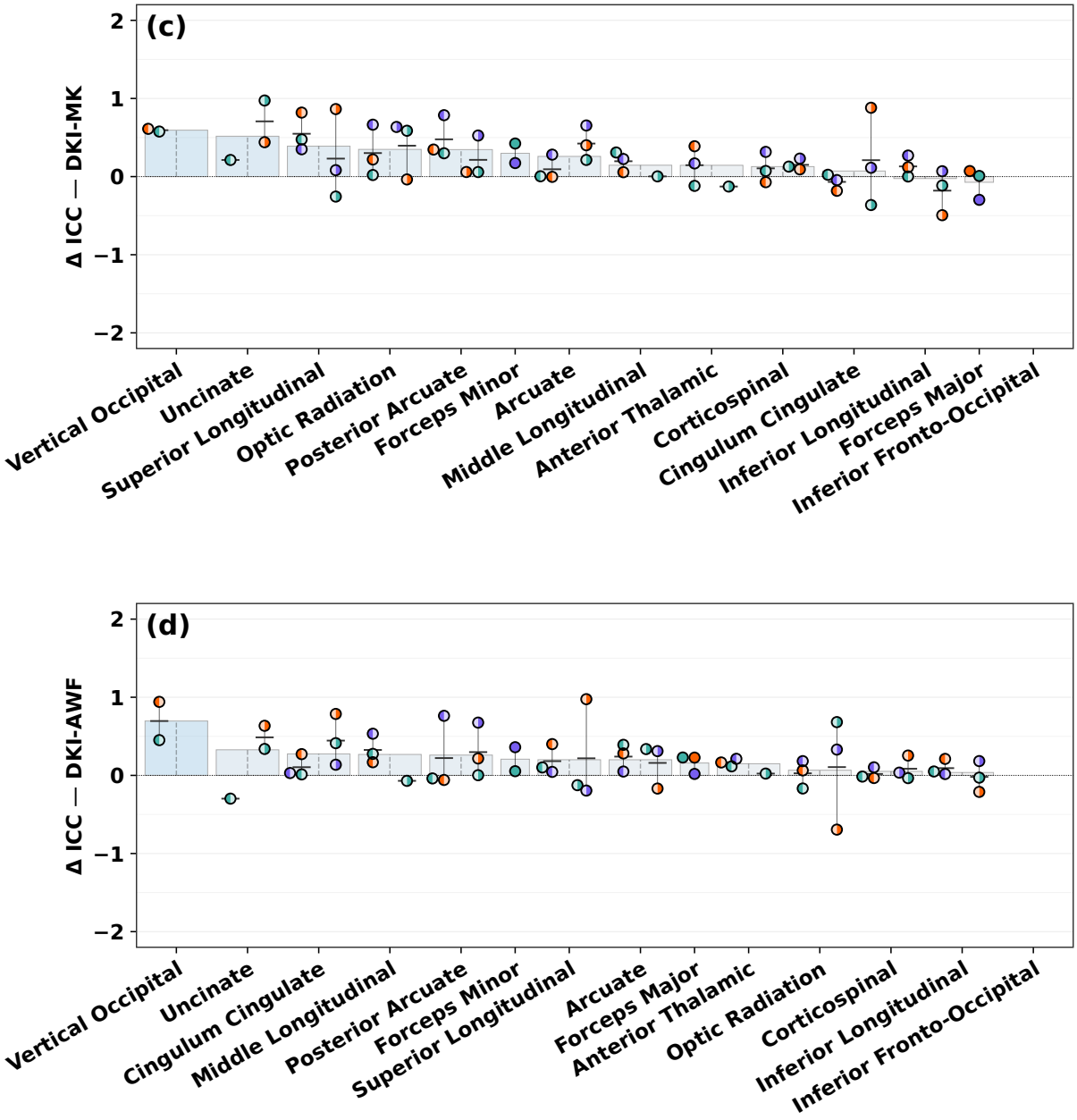

When averaged across tracts with paired estimates, ICC increased following babyFWE for all four tissue properties. The mean raw difference was 0.19 for DKI-FA (SD = 0.20), 0.19 for DKI-MD (SD = 0.20), 0.24 for DKI-MK (SD = 0.20), and 0.22 for DKI-AWF (SD = 0.17). Complete participant- and tract-level values are reported in Tables D.1, E.1, F.1, and G.1.

3.2 Tract Yield

Tract yield was assessed using whole-brain, non-split tractography. Averaged across the 14 tracts, yield was higher following babyFWE (100.0%, SD = 0.0%) than for the conventional pipeline (69.0%, SD = 37.5%). The corresponding mean yield difference was 31.0% (SD = 37.5%); tract-specific values are reported in Table H.1.

Yield increased for 7 of the 14 tracts, with no tract exhibiting a negative mean yield difference (Fig. 3.4). The largest improvement was observed for the vertical occipital fasciculus (100.0%, SD = 0.0%), followed by the inferior fronto-occipital fasciculus (83.3%, SD = 28.9%), posterior arcuate (83.3%, SD = 28.9%), and uncinate fasciculus (66.7%, SD = 57.7%). The remaining seven tracts showed no change in yield because they were successfully reconstructed by both pipelines.

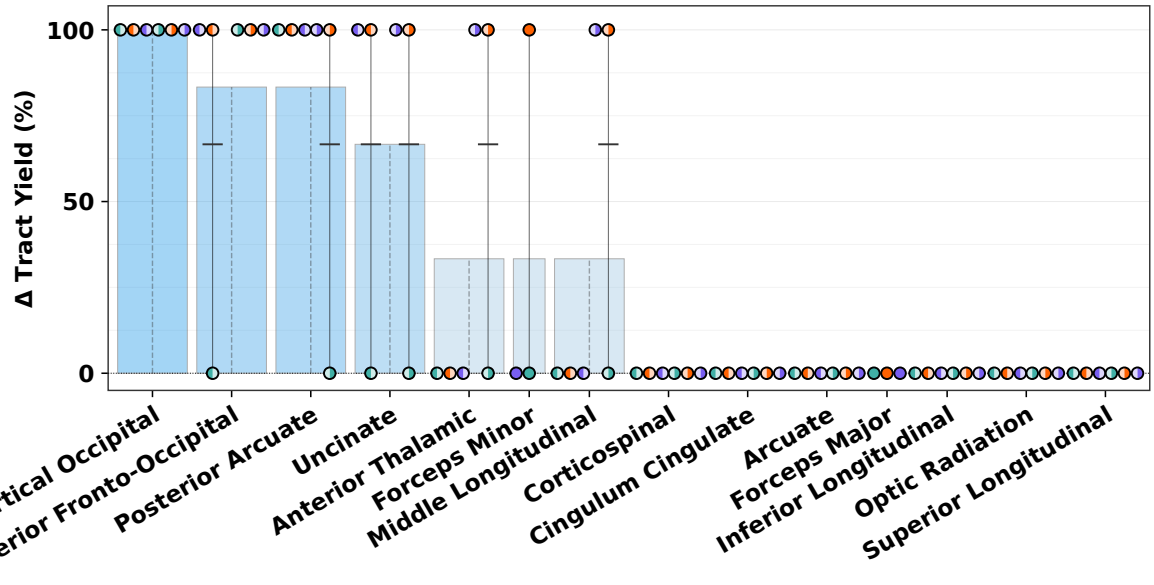

Figure 3.4: Change in tract yield following babyFWE. Bars represent the mean percentage-point difference for each tract, with points indicating participant-level values.

4 Discussion

4.1 Principal Findings

This study evaluated the effect of free-water elimination on neonatal tractometry by benchmarking its impact across multiple stages of the tractometry pipeline, including fiber-orientation distribution functions (fODFs), tract delineation, tract-profile reliability, and tract yield. Collectively, babyFWE generally improved the stability of tract-based analyses relative to the conventional pipeline, although the magnitude of improvement differed among outcome measures.

The most consistent improvements were observed for tract delineation and tract yield. Weighted Dice coefficients increased for all evaluated tracts, while tract yield improved for half of the evaluated tracts without any reduction in yield. Voxelwise fODF reliability also generally improved, although the magnitude of change was modest and spatially heterogeneous. Similarly, tract-profile reliability also improved, although the effect was modest and differed among tissue properties and tracts. These findings suggest that free-water elimination can improve the reliability of neonatal tractometry throughout the processing pipeline.

4.2 Interpretation

The improvements observed throughout this study are consistent with the underlying biological characteristics of the developing brain. Compared with adults, neonatal WM contains substantially more free water due to its immature microstructural organization, including incomplete myelination and reduced tissue packing (Dubois et al., 2014; Ouyang et al., 2019). This elevated free-water content increases susceptibility to partial-volume contamination from cerebrospinal fluid (CSF) and extracellular water. Consequently, diffusion measurements within individual voxels represent a mixture of anisotropic WM diffusion and isotropically diffusing free water, reducing the specificity of tissue-derived measurements and the reliability of subsequent tract-based analyses.

FWE is designed to address this source of measurement uncertainty by modeling the diffusion

signal as separate isotropic free-water and anisotropic tissue compartments (Pasternak et al., 2009). By reducing the contribution of isotropically diffusing free water, the remaining signal is expected to better reflect the underlying WM microstructure. The improvements in reliability observed throughout this study are consistent with this proposed mechanism, suggesting that reducing free-water contamination can produce more reproducible measurements of developing WM.

Although reliability generally improved following babyFWE, the pattern of improvement differed among outcome measures. This variation is consistent with prior tractometry research showing that spatial bundle agreement and tract-profile reliability capture related but non-equivalent properties of the analysis (Kruper et al., 2021). The pronounced improvements in tract delineation and yield may reflect the capacity of FWE to preserve directional diffusion information that could otherwise be obscured by isotropic free-water contamination, consistent with prior evidence that FWE can support streamline continuity and more complete pathway reconstruction in regions with elevated free water (Chang et al., 2025).

However, the pattern of improvement observed in neonates differed from that reported in aging brains, where elevated free water is often associated with localized pathological tissue changes (Chang et al., 2025). In contrast, elevated free water in neonatal WM is more broadly distributed throughout the developing brain, reflecting immature tissue composition, incomplete myelination, and ongoing microstructural development (Gullett et al., 2020; Dubois et al., 2014; Ouyang et al., 2019). FWE may therefore act on a more widely distributed source of isotropic signal throughtout neonatal WM rather than primarily within discrete regions of elevated free water. This difference may contribute to the more heterogeneous effects observed in the present study, with the magnitude and direction of change varying across voxels, tracts, and outcome measures.

These findings support further investigation of FWE as a preprocessing strategy for neonatal tractometry. Improved reliability may reduce non-biological variability and increase sensitivity to developmental differences in both cross-sectional and longitudinal studies. As large-scale infant neuroimaging datasets continue to expand, robust tractometry pipelines will be increasingly important for characterizing early WM development and identifying alterations associated with neurodevelopmental conditions.

4.3 Limitations

The primary limitation of this study is the small sample size. Although the split-half design enabled reliability to be evaluated within each participant, the study included only 3 neonates. Therefore, the estimated effects should be interpreted cautiously and cannot yet be assumed to generalize to the broader neonatal population. Nevertheless, the improvements observed across multiple components of the tractometry pipeline provide a basis for further investigation of FWE in larger cohorts.

The study was also limited to a single cohort from one publicly available dataset. Differences in developmental stage, clinical characteristics, scanner hardware, and diffusion acquisition protocols may influence both free-water estimation and its effects on tractometry. Validation across independent datasets and more diverse neonatal populations will therefore be necessary to establish the generalizability of these findings.

In addition, the results are specific to the models and processing procedures implemented in the present pipeline. The effects of FWE may differ when paired with alternative reconstruction methods, tractography algorithms, bundle-segmentation approaches, or tissue-property models. Accordingly, the present findings should not be interpreted as evidence that FWE will produce equivalent improvements across all neonatal dMRI pipelines.

Finally, this study evaluated measurement reliability rather than biological accuracy. More reproducible estimates are not necessarily more accurate representations of the underlying WM microstructure or anatomical connectivity. Independent validation using simulations, physical phantoms (Farrher et al., 2020), anatomical reference data, or established developmental associations will be needed to determine whether the observed reliability improvements also correspond to greater biological validity.

4.4 Future Directions

The immediate priority for future work is to extend this proof-of-concept evaluation to a larger and more diverse neonatal cohort within the Developing Human Connectome Project (Edwards et al., 2022) through a Preregistered Research Report (PRR). This larger evaluation will provide a more rigorous assessment of the reliability improvements observed in the present study. Subsequent validation across

independent datasets, scanners, acquisition protocols, and developmental stages will be necessary to determine the broader generalizability of babyFWE. Large-scale longitudinal resources, including the Baby Connectome Project and HEALthy Brain and Child Development Study, provide opportunities to evaluate babyFWE across early development and determine whether the effects of FWE vary with age, tissue maturation, or acquisition characteristics (Howell et al., 2019; Nelson et al., 2024).

Future studies should also move beyond reliability to evaluate biological and clinical validity. Downstream analyses could determine whether babyFWE-derived measurements improve sensitivity to established developmental differences, prediction of chronological age (Sun et al., 2024), or discrimination between infants born preterm and at term (Pecheva et al., 2017). Longitudinal analyses could further assess whether improved tractometry reliability strengthens the characterization of individual developmental trajectories or improves prediction of later neurodevelopmental outcomes.

A broader objective is to incorporate babyFWE into a modular, open-source software ecosystem for neonatal dMRI. Within this framework, FWE could be integrated with complementary methods for asymmetric fiber-orientation modeling (Bastiani et al., 2017), anatomically constrained tractography (Smith et al., 2012), and tract-profile analysis. These tools could be implemented independently according to the requirements of a particular dataset or combined to address multiple sources of measurement uncertainty within a unified tract-based analysis framework. Standardized validation benchmarks, documented implementation guidelines, and interoperable software would support reproducibility and facilitate adoption across the infant neuroimaging community.

Ultimately, improved neonatal tractometry may contribute to earlier and more precise characterization of atypical WM development. dMRI and tractography have shown promise for relating WM organization to motor function and cerebral palsy, particularly through characterization of the corticospinal and somatosensory pathways (Mailleux et al., 2020). Diffusion abnormalities in the neonatal corticospinal tract have also been associated with later motor outcomes following perinatal brain injury (Kirton et al., 2007). Future work should therefore examine whether more reliable tractometry can improve prognostic models, identify infants who may benefit from earlier intervention, and provide quantitative markers for monitoring developmental or rehabilitative outcomes.

Advances in large-scale infant neuroimaging datasets create both an opportunity and a methodological challenge. These resources have the potential to transform understanding of early brain development, but realizing that potential will require computational tools that are reliable, transparent, and adapted to the developing brain. Continued development of babyFWE and the broader software ecosystem may help bridge this gap by providing a validated foundation for reproducible neonatal tractometry.

4.5 Conclusions

This study benchmarked the effect of FWE across multiple components of a neonatal tractometry pipeline. babyFWE generally improved reliability relative to conventional processing, with particularly consistent gains in tract delineation and tract yield and more variable improvements in voxelwise fODF and tract-profile reliability. These findings provide preliminary evidence that reducing isotropic free-water contamination can improve the reliability of tract-based measurements in the developing brain.

Although further validation is needed, these findings establish a promising foundation for integrating FWE into neonatal dMRI pipelines. By improving the reliability with which early WM development can be measured, methods such as babyFWE may ultimately support more sensitive developmental research, earlier identification of infants at risk for adverse outcomes, and more informed evaluation of interventions intended to improve lifelong neurological health.

Bibliography

Barkovich, M. J., Li, Y., Desikan, R. S., Barkovich, A. J., and Xu, D. (2019). Challenges in pediatric neuroimaging. *NeuroImage*, 185:793–801.

Bastiani, M., Andersson, J. L. R., Cordero-Grande, L., Murgasova, M., Hutter, J., Price, A. N., Makropoulos, A., Fitzgibbon, S. P., Hughes, E., Rueckert, D., Victor, S., Rutherford, M., Edwards, A. D., Smith, S. M., Tournier, J.-D., Hajnal, J. V., Jbabdi, S., and Sotiropoulos, S. N. (2019). Automated processing pipeline for neonatal diffusion MRI in the developing Human Connectome Project. *NeuroImage*, 185:750–763.

Bastiani, M., Cottaar, M., Dikranian, K., Ghosh, A., Zhang, H., Alexander, D. C., Behrens, T. E., Jbabdi, S., and Sotiropoulos, S. N. (2017). Improved tractography using asymmetric fibre orientation distributions. *NeuroImage*, 158:205–218.

Beaulieu, C. (2002). The basis of anisotropic water diffusion in the nervous system - a technical review. *NMR in biomedicine*, 15(7-8):435–455.

Chang, K., Burke, L., LaPiana, N., Howlett, B., Hunt, D., Dezelar, M., Andre, J. B., Curl, P., Ralston, J. D., Rokem, A., and Mac Donald, C. L. (2025). Free water elimination tractometry for aging brains. *Imaging Neuroscience*, 3:IMAG.a.991.

Cordero-Grande, L., Ferrazzi, G., Teixeira, R. P. A. G., O'Muircheartaigh, J., Price, A. N., and Hajnal, J. V. (2020). Motion-corrected MRI with DISORDER: Distributed and incoherent sample orders for reconstruction deblurring using encoding redundancy. *Magnetic Resonance in Medicine*, 84(2):713–726.

Cordero-Grande, L., Hughes, E. J., Hutter, J., Price, A. N., and Hajnal, J. V. (2018). Three-dimensional motion corrected sensitivity encoding reconstruction for multi-shot multi-slice MRI: Application to neonatal brain imaging. *Magnetic Resonance in Medicine*, 79(3):1365–1376.

Correia, M. M., Henriques, R. N., Golub, M., Winzeck, S., and Nunes, R. G. (2024). The trouble with free-water elimination using single-shell diffusion MRI data: A case study in ageing. *Imaging Neuroscience*, 2:imag–2–00252.

Cousineau, M., Jodoin, P.-M., Garyfallidis, E., Côté, M.-A., Morency, F. C., Rozanski, V., Grand'Maison, M., Bedell, B. J., and Descoteaux, M. (2017). A test-retest study on Parkinson's PPMI dataset yields statistically significant white matter fascicles. *NeuroImage: Clinical*, 16:222–233.

Doi, M., Usui, N., and Shimada, S. (2022). Prenatal Environment and Neurodevelopmental Disorders. *Frontiers in Endocrinology*, 13:860110.

Dubois, J., Dehaene-Lambertz, G., Kulikova, S., Poupon, C., Hüppi, P. S., and Hertz-Pannier, L. (2014). The early development of brain white matter: A review of imaging studies in fetuses, newborns and infants. *Neuroscience*, 276:48–71.

Edwards, A. D., Rueckert, D., Smith, S. M., Abo Seada, S., Alansary, A., Almalbis, J., Allsop, J., Andersson, J., Arichi, T., Arulkumaran, S., Bastiani, M., Batalle, D., Baxter, L., Bozek, J., Braithwaite, E., Brandon, J., Carney, O., Chew, A., Christiaens, D., Chung, R., Colford, K., Cordero-Grande, L., Counsell, S. J., Cullen, H., Cupitt, J., Curtis, C., Davidson, A., Deprez, M., Dillon, L., Dimitrakopoulou, K., Dimitrova, R., Duff, E., Falconer, S., Farahibozorg, S.-R., Fitzgibbon, S. P., Gao, J., Gaspar, A., Harper, N., Harrison, S. J., Hughes, E. J., Hutter, J., Jenkinson, M., Jbabdi, S., Jones, E., Karolis, V., Kyriakopoulou, V., Lenz, G., Makropoulos, A., Malik, S., Mason, L., Mortari, F., Nosarti, C., Nunes, R. G., O'Keeffe, C., O'Muircheartaigh, J., Patel, H., Passerat-Palmbach, J., Pietsch, M., Price, A. N., Robinson, E. C., Rutherford, M. A., Schuh, A., Sotiropoulos, S., Steinweg, J., Teixeira, R. P. A. G., Tenev, T., Tournier, J.-D., Tusor, N., Uus, A., Vecchiato, K., Williams, L. Z. J., Wright, R., Wurie, J., and Hajnal, J. V. (2022). The Developing Human Connectome Project Neonatal Data Release. *Frontiers in Neuroscience*, 16.

Farrher, E., Grinberg, F., Kuo, L.-W., Cho, K.-H., Buschbeck, R. P., Chen, M.-J., Chiang, H.-H., Choi, C.-H., and Shah, N. J. (2020). Dedicated diffusion phantoms for the investigation of free water elimination and mapping: Insights into the influence of T2 relaxation properties. *NMR in Biomedicine*, 33(4):e4210.

Fieremans, E., Jensen, J. H., and Helpern, J. A. (2011). White matter characterization with diffusional kurtosis imaging. *NeuroImage*, 58(1):177–188.

Fitzgibbon, S. P., Harrison, S. J., Jenkinson, M., Baxter, L., Robinson, E. C., Bastiani, M., Bozek, J., Karolis, V., Cordero Grande, L., Price, A. N., Hughes, E., Makropoulos, A., Passerat-Palmbach, J., Schuh, A., Gao, J., Farahibozorg, S.-R., O'Muircheartaigh, J., Ciarrusta, J., O'Keeffe, C., Brandon, J., Arichi, T., Rueckert, D., Hajnal, J. V., Edwards, A. D., Smith, S. M., Duff, E., and Andersson, J. (2020). The developing Human Connectome Project (dHCP) automated resting-state functional processing framework for newborn infants. *Neuroimage*, 223:117303.

Forkel, S. J., Friedrich, P., Thiebaut de Schotten, M., and Howells, H. (2022). White matter variability, cognition, and disorders: A systematic review. *Brain Structure & Function*, 227(2):529–544.

Francés, L., Quintero, J., Fernández, A., Ruiz, A., Caules, J., Fillon, G., Hervás, A., and Soler, C. V. (2022). Current state of knowledge on the prevalence of neurodevelopmental disorders in childhood according to the DSM-5: A systematic review in accordance with the PRISMA criteria. *Child and Adolescent Psychiatry and Mental Health*, 16:27.

Garyfallidis, E., Brett, M., Amirbekian, B., Rokem, A., van der Walt, S., Descoteaux, M., and Nimmo-Smith, I. (2014). Dipy, a library for the analysis of diffusion MRI data. *Frontiers in Neuroinformatics*, 8:8.

Gilmore, J. H., Knickmeyer, R. C., and Gao, W. (2018). Imaging structural and functional brain development in early childhood. *Nature Reviews. Neuroscience*, 19(3):123–137.

Golub, M., Neto Henriques, R., and Gouveia Nunes, R. (2021). Free-water DTI estimates from single b-value data might seem plausible but must be interpreted with care. *Magnetic Resonance in Medicine*, 85(5):2537–2551.

Grotheer, M., Bloom, D., Kruper, J., Richie-Halford, A., Zika, S., Aguilera González, V. A., Yeatman, J. D., Grill-Spector, K., and Rokem, A. (2023). Human white matter myelinates faster in utero than ex utero. *Proceedings of the National Academy of Sciences*, 120(33):e2303491120.

Grotheer, M., Rosenke, M., Wu, H., Kular, H., Querdasi, F. R., Natu, V. S., Yeatman, J. D., and Grill-Spector, K. (2022). White matter myelination during early infancy is linked to spatial gradients and myelin content at birth. *Nature Communications*, 13(1):997.

Gullett, J. M., O'Shea, A., Lamb, D. G., Porges, E. C., O'Shea, D. M., Pasternak, O., Cohen, R. A., and Woods, A. J. (2020). The association of white matter free water with cognition in older adults. *NeuroImage*, 219:117040.

Hennel, F., Buehrer, M., von Deuster, C., Seuven, A., and Pruessmann, K. P. (2016). SENSE reconstruction for multiband EPI including slice-dependent N/2 ghost correction. *Magnetic Resonance in Medicine*, 76(3):873–879.

Henriques, R. N., Correia, M. M., Marrale, M., Huber, E., Kruper, J., Koudoro, S., Yeatman, J. D., Garyfallidis, E., and Rokem, A. (2021). Diffusional Kurtosis Imaging in the Diffusion Imaging in Python Project. *Frontiers in Human Neuroscience*, 15:675433.

Henriques, R. N., Rokem, A., Garyfallidis, E., St-Jean, S., Peterson, E. T., and Correia, M. M. (2017). [Re] Optimization of a free water elimination two-compartment model for diffusion tensor imaging. *ReScience*, 3(1).

Howell, B. R., Styner, M. A., Gao, W., Yap, P.-T., Wang, L., Baluyot, K., Yacoub, E., Chen, G., Potts, T., Salzwedel, A., Li, G., Gilmore, J. H., Piven, J., Smith, J. K., Shen, D., Ugurbil, K., Zhu, H., Lin, W., and Elison, J. T. (2019). The UNC/UMN Baby Connectome Project (BCP): An Overview of the Study Design and Protocol Development. *NeuroImage*, 185:891–905.

Hoy, A. R., Koay, C. G., Kecskemeti, S. R., and Alexander, A. L. (2014). Optimization of a Free Water Elimination Two-Compartment Model for Diffusion Tensor Imaging. *NeuroImage*, 103:323–333.

Hughes, E. J., Winchman, T., Padormo, F., Teixeira, R., Wurie, J., Sharma, M., Fox, M., Hutter, J., Cordero-Grande, L., Price, A. N., Allsop, J., Bueno-Conde, J., Tusor, N., Arichi, T., Edwards, A. D., Rutherford, M. A., Counsell, S. J., and Hajnal, J. V. (2017). A dedicated neonatal brain imaging system. *Magnetic Resonance in Medicine*, 78(2):794–804.

Hutter, J., Christiaens, D. J., Schneider, T., Cordero-Grande, L., Slator, P. J., Deprez, M., Price, A. N., Tournier, J.-D., Rutherford, M., and Hajnal, J. V. (2018a). Slice-level diffusion encoding for motion and distortion correction. *Medical Image Analysis*, 48:214–229.

Hutter, J., Tournier, J. D., Price, A. N., Cordero-Grande, L., Hughes, E. J., Malik, S., Steinweg, J., Bastiani, M., Sotiropoulos, S. N., Jbabdi, S., Andersson, J., Edwards, A. D., and Hajnal, J. V. (2018b). Time-efficient and flexible design of optimized multishell HARDI diffusion. *Magnetic Resonance in Medicine*, 79(3):1276–1292.

Jensen, J. H., Helpern, J. A., Ramani, A., Lu, H., and Kaczynski, K. (2005). Diffusional kurtosis imaging: The quantification of non-gaussian water diffusion by means of magnetic resonance imaging. *Magnetic Resonance in Medicine*, 53(6):1432–1440.

Jeurissen, B., Descoteaux, M., Mori, S., and Leemans, A. (2019). Diffusion MRI fiber tractography of the brain. *NMR in Biomedicine*, 32(4):e3785.

Kirton, A., Shroff, M., Visvanathan, T., and deVeber, G. (2007). Quantified corticospinal tract diffusion restriction predicts neonatal stroke outcome. *Stroke*, 38(3):974–980.

Knickmeyer, R. C., Gouttard, S., Kang, C., Evans, D., Wilber, K., Smith, J. K., Hamer, R. M., Lin, W., Gerig, G., and Gilmore, J. H. (2008). A Structural MRI Study of Human Brain Development from Birth to 2 Years. *The Journal of Neuroscience*, 28(47):12176–12182.

Kruper, J., Richie-Halford, A., Qiao, J., Gilmore, A., Chang, K., Grotheer, M., Roy, E., Caffarra, S., Gomez, T., Chou, S., Cieslak, M., Koudoro, S., Garyfallidis, E., Satterthwaite, T. D., Yeatman, J. D., and Rokem, A. (2025). A software ecosystem for brain tractometry processing, analysis, and insight. *PLOS Computational Biology*, 21(8):e1013323.

Kruper, J., Yeatman, J. D., Richie-Halford, A., Bloom, D., Grotheer, M., Caffarra, S., Kiar, G., Karipidis, I. I., Roy, E., Chandio, B. Q., Garyfallidis, E., and Rokem, A. (2021). Evaluating the Reliability of Human Brain White Matter Tractometry. *Aperture Neuro*, 1(1).

Lebel, C. and Deoni, S. (2018). The Development of Brain White Matter Microstructure. *NeuroImage*, 182:207–218.

Mailleux, L., Franki, I., Emsell, L., Peedima, M.-L., Fehrenbach, A., Feys, H., and Ortibus, E. (2020). The relationship between neuroimaging and motor outcome in children with cerebral palsy: A systematic review-Part B diffusion imaging and tractography. *Research in Developmental Disabilities*, 97:103569.

Matsuzawa, J., Matsui, M., Konishi, T., Noguchi, K., Gur, R. C., Bilker, W., and Miyawaki, T. (2001). Age-related volumetric changes of brain gray and white matter in healthy infants and children. *Cerebral Cortex*, 11(4):335–342.

McMaster, E. M., Newlin, N. R., Cho, C., Rudravaram, G., Saunders, A. M., Krishnan, A. R., Remedios, L. W., Kim, M. E., Xu, H., Schilling, K. G., Rheault, F., Cutting, L. E., and Landman, B. A. (2025). Sensitivity of quantitative diffusion MRI tractography and microstructure to anisotropic spatial sampling. *Magnetic Resonance Imaging*, 124:110539.

Nelson, C. A., Frankeberger, J., and Chambers, C. D. (2024). An introduction to the HEALthy Brain and Child Development Study (HBCD) study. *Developmental Cognitive Neuroscience*, 69:101441.

Olusanya, B. O., Smythe, T., Ogbo, F. A., Nair, M. K. C., Scher, M., and Davis, A. C. (2023). Global prevalence of developmental disabilities in children and adolescents: A systematic umbrella review. *Frontiers in Public Health*, 11:1122009.

Ouyang, M., Dubois, J., Yu, Q., Mukherjee, P., and Huang, H. (2019). Delineation of early brain development from fetuses to infants with diffusion MRI and beyond. *NeuroImage*, 185:836–850.

Pasternak, O., Sochen, N., Gur, Y., Intrator, N., and Assaf, Y. (2009). Free water elimination and mapping from diffusion MRI. *Magnetic Resonance in Medicine*, 62(3):717–730.

Pecheva, D., Yushkevich, P., Batalle, D., Hughes, E., Aljabar, P., Wurie, J., Hajnal, J. V., Edwards, A. D., Alexander, D. C., Counsell, S. J., and Zhang, H. (2017). A tract-specific approach to assessing white matter in preterm infants. *NeuroImage*, 157:675–694.

Pierpaoli, C. and Jones, D. K. (2004). Removing CSF Contamination in Brain DT-MRIs by Using a Two-Compartment Tensor Model. In *Proceedings of the International Society for Magnetic Resonance in Medicine*, page 1215, Kyoto, Japan.

Rokem, A., Yeatman, J. D., Pestilli, F., Kay, K. N., Mezer, A., van der Walt, S., and Wandell, B. A. (2015). Evaluating the Accuracy of Diffusion MRI Models in White Matter. *PLoS ONE*, 10(4):e0123272.

Schilling, K. G., Nath, V., Hansen, C., Parvathaneni, P., Blaber, J., Gao, Y., Neher, P., Aydogan, D. B., Shi, Y., Ocampo-Pineda, M., Schiavi, S., Daducci, A., Girard, G., Barakovic, M., Rafael-Patino, J., Romascano, D., Rensonnet, G., Pizzolato, M., Bates, A., Fischi, E., Thiran, J.-P., Canales-Rodríguez, E. J., Huang, C., Zhu, H., Zhong, L., Cabeen, R., Toga, A. W., Rheault, F., Theaud, G., Houde, J.-C., Sidhu, J., Chamberland, M., Westin, C.-F., Dyrby, T. B., Verma, R., Rathi, Y., Irfanoglu, M. O., Thomas, C., Pierpaoli, C., Descoteaux, M., Anderson, A. W., and Landman, B. A. (2019). Limits to anatomical accuracy of diffusion tractography using modern approaches. *NeuroImage*, 185:1–11.

Smith, R. E., Tournier, J.-D., Calamante, F., and Connelly, A. (2012). Anatomically-constrained tractography: Improved diffusion MRI streamlines tractography through effective use of anatomical information. *NeuroImage*, 62(3):1924–1938.

Sun, H., Mehta, S., Khaitova, M., Cheng, B., Hao, X., Spann, M., and Scheinost, D. (2024). Brain age prediction and deviations from normative trajectories in the neonatal connectome. *Nature Communications*, 15(1):10251.

Tournier, J.-D., Calamante, F., and Connelly, A. (2007). Robust determination of the fibre orientation distribution in diffusion MRI: Non-negativity constrained super-resolved spherical deconvolution. *NeuroImage*, 35(4):1459–1472.

Tournier, J.-D., Christiaens, D., Hutter, J., Price, A. N., Cordero-Grande, L., Hughes, E., Bastiani, M., Sotiropoulos, S. N., Smith, S. M., Rueckert, D., Counsell, S. J., Edwards, A. D., and Hajnal, J. V. (2020). A data-driven approach to optimising the encoding for multi-shell diffusion MRI with application to neonatal imaging. *NMR in biomedicine*, 33(9):e4348.

Vallat, R. (2018). Pingouin: Statistics in Python. *Journal of Open Source Software*, 3(31):1026.

Yeatman, J. D., Dougherty, R. F., Myall, N. J., Wandell, B. A., and Feldman, H. M. (2012). Tract Profiles of White Matter Properties: Automating Fiber-Tract Quantification. *PLoS ONE*, 7(11):e49790.

Zhang, F., Daducci, A., He, Y., Schiavi, S., Seguin, C., Smith, R. E., Yeh, C.-H., Zhao, T., and O'Donnell, L. J. (2022). Quantitative mapping of the brain's structural connectivity using diffusion MRI tractography: A review. *NeuroImage*, 249:118870.

Zhao, Y., Yang, L., Gong, G., Cao, Q., and Liu, J. (2022). Identify aberrant white matter microstructure in ASD, ADHD and other neurodevelopmental disorders: A meta-analysis of diffusion tensor imaging studies. *Progress in Neuro-Psychopharmacology and Biological Psychiatry*, 113:110477.

Zhu, K., Dougherty, R. F., Wu, H., Middione, M. J., Takahashi, A. M., Zhang, T., Pauly, J. M., and Kerr, A. B. (2016). Hybrid-Space SENSE Reconstruction for Simultaneous Multi-Slice MRI. *IEEE transactions on medical imaging*, 35(8):1824–1836.

A Participant Summary

Table A.1: Participant codes, identifiers, and colors used throughout the analysis.

Color	Code ID	Participant ID	Session ID
●	C1	sub-CC00720XX11	ses-211101
●	C2	sub-CC00549XX22	ses-157600
●	C3	sub-CC00339XX18	ses-107200

B Fiber-Orientation Distribution Function Reliability (r^2)

Table B.1: fODF split-half reliability (r^2) and symmetric percent change for the conventional and babyFWE pipelines. For each participant, reliability was summarized as the mean and median of the voxelwise r^2 values within WM ($n = 3$; see Methods, Results, and Figure 3.1).

Color	ID	Mean Voxelwise r^2			Median Voxelwise r^2		
		DWI	**FWE**	**Δ (%)**	**DWI**	**FWE**	**Δ (%)**
●	C1	0.36 (0.15)	0.34 (0.16)	−8.2 (23.9)	0.35 (0.20)	0.33 (0.22)	−2.7 (13.8)
●	C2*	0.06 (0.13)	0.07 (0.14)	9.6 (63.5)	0.02 (0.05)	0.02 (0.06)	5.6 (35.8)
●	C3	0.06 (0.12)	0.07 (0.14)	22.5 (70.8)	0.01 (0.04)	0.01 (0.06)	19.0 (50.8)
●	G	0.16 (0.17)	0.16 (0.16)	8.0 (15.4)	0.12 (0.19)	0.12 (0.18)	7.3 (10.9)

Note. Participant rows report the mean or median of each participant's voxelwise WM distribution, with SD or IQR, respectively; G reports the group mean (SD). The asterisk identifies the representative participant featured in Figure 3.1.

C Tract Delineation Reliability (Dice)

Table C.1: Weighted Dice coefficients for the conventional and babyFWE pipelines, with symmetric percent change, for each participant and tract ($n = 3$; see Methods and Results, Figure 3.2).

Tract	Laterality	Color	ID	Dice		
				DWI	FWE	Δ (%)
Anterior Thalamic	◐	●	C1	0.51	0.69	29.0
		●	C2	0.48	0.60	22.7
		●	C3	0.16	0.73	128.4
		●	G	0.38 (0.19)	0.67 (0.07)	60.0 (59.3)
	◑	●	C1	–	0.34	–
		●	C2	0.58	0.64	10.1
		●	C3	–	0.22	–
		●	G	0.58	0.40 (0.22)	10.1
	○	●	C1	0.51	0.51	29.0
		●	C2	0.53	0.62	16.4
		●	C3	0.16	0.48	128.4
		●	G	0.40 (0.21)	0.54 (0.08)	57.9 (61.4)
Arcuate	◐	●	C1	0.49	0.67	31.1
		●	C2	0.45	0.72	46.3
		●	C3	0.24	0.62	89.4
		●	G	0.39 (0.14)	0.67 (0.05)	55.6 (30.2)
	◑	●	C1	0.27	0.53	64.9
		●	C2	0.45	0.53	16.6
		●	C3	0.03	0.34	162.8
		●	G	0.25 (0.21)	0.47 (0.11)	81.4 (74.5)
	○	●	C1	0.38	0.60	48.0
		●	C2	0.45	0.62	31.5
		●	C3	0.14	0.48	126.1
		●	G	0.32 (0.16)	0.57 (0.08)	68.5 (50.5)
Cingulum Cingulate	◐	●	C1	0.31	0.66	71.1
		●	C2	0.67	0.43	−42.5
		●	C3	0.70	0.70	−0.0
		●	G	0.56 (0.21)	0.60 (0.14)	9.5 (57.4)
	◑	●	C1	0.08	0.50	147.2
		●	C2	0.16	0.22	31.7
		●	C3	0.04	0.21	133.3
		●	G	0.09 (0.06)	0.31 (0.17)	104.1 (63.1)
	○	●	C1	0.20	0.58	109.2
		●	C2	0.41	0.32	−5.4
		●	C3	0.37	0.45	66.6
		●	G	0.33 (0.12)	0.45 (0.13)	56.8 (57.9)

continued on next page

Table C.1: Tract Delineation (Dice) Summary — continued from previous page

Tract	Laterality	Color	ID	Dice		
				DWI	FWE	Δ (%)
Corticospinal	◐		C_1	0.90	0.87	−2.6
			C_2	0.84	0.86	2.7
			C_3	0.74	0.84	11.7
			G	0.83 (0.08)	0.86 (0.02)	3.9 (7.2)
	◑		C_1	0.84	0.82	−1.9
			C_2	0.86	0.89	3.8
			C_3	0.36	0.72	66.7
			G	0.68 (0.28)	0.81 (0.09)	22.9 (38.1)
	○		C_1	0.87	0.85	−2.2
			C_2	0.85	0.88	3.2
			C_3	0.55	0.78	39.2
			G	0.76 (0.18)	0.83 (0.05)	13.4 (22.5)
Forceps Major	●		C_1	0.84	0.92	9.3
			C_2	0.09	0.61	148.7
			C_3	0.62	0.79	24.1
			G	0.52 (0.39)	0.78 (0.16)	60.7 (76.6)
Forceps Minor	●		C_1	0.54	0.91	50.6
			C_2	0.84	0.86	1.5
			C_3	–	0.10	–
			G	0.69 (0.21)	0.62 (0.45)	26.1 (34.7)
Inferior Fronto-Occipital	◐		C_1	–	0.26	–
			C_2	–	0.34	–
			C_3	–	0.27	–
			G	–	0.29 (0.05)	–
	◑		C_1	–	0.35	–
			C_2	–	0.29	–
			C_3	–	0.05	–
			G	–	0.23 (0.16)	–
	○		C_1	–	0.30	–
			C_2	–	0.31	–
			C_3	–	0.16	–
			G	–	0.26 (0.08)	–

continued on next page

Table C.1: Tract Delineation (Dice) Summary — continued from previous page

Tract	Laterality	Color	ID	Dice		
				DWI	FWE	Δ (%)
Inferior Longitudinal	◐	●	C_1	0.69	0.88	24.3
		●	C_2	0.79	0.88	11.2
		●	C_3	0.47	0.86	58.7
		●	G	0.65 (0.16)	0.88 (0.01)	31.4 (24.5)
	◑	●	C_1	0.54	0.83	41.6
		●	C_2	0.68	0.88	25.6
		●	C_3	0.67	0.69	3.9
		●	G	0.63 (0.08)	0.80 (0.10)	23.7 (18.9)
	○	●	C_1	0.62	0.86	33.0
		●	C_2	0.74	0.88	18.4
		●	C_3	0.57	0.78	31.3
		●	G	0.64 (0.09)	0.84 (0.05)	27.6 (8.0)
Middle Longitudinal	◐	●	C_1	0.28	0.47	50.6
		●	C_2	0.48	0.83	54.3
		●	C_3	0.14	0.76	137.5
		●	G	0.30 (0.17)	0.69 (0.19)	80.8 (49.1)
	◑	●	C_1	–	0.65	–
		●	C_2	0.25	0.51	68.1
		●	C_3	–	0.18	–
		●	G	0.25	0.45 (0.24)	68.1
	○	●	C_1	0.28	0.56	50.6
		●	C_2	0.36	0.67	61.2
		●	C_3	0.14	0.47	137.5
		●	G	0.26 (0.11)	0.57 (0.10)	83.1 (47.4)
Optic Radiation	◐	●	C_1	0.65	0.75	13.5
		●	C_2	0.20	0.33	50.7
		●	C_3	0.27	0.34	23.7
		●	G	0.37 (0.25)	0.47 (0.24)	29.3 (19.3)
	◑	●	C_1	0.38	0.52	30.2
		●	C_2	0.13	0.28	72.2
		●	C_3	0.27	0.06	−127.4
		●	G	0.26 (0.13)	0.28 (0.23)	−8.3 (105.2)
	○	●	C_1	0.52	0.63	21.8
		●	C_2	0.16	0.30	61.4
		●	C_3	0.27	0.20	−51.8
		●	G	0.32 (0.18)	0.38 (0.23)	10.5 (57.5)

continued on next page

Table C.1: Tract Delineation (Dice) Summary — continued from previous page

Tract	Laterality	Color	ID	Dice		
				DWI	FWE	Δ (%)
Posterior Arcuate	◐		C1	0.14	0.63	127.7
			C2	0.17	0.58	109.8
			C3	0.01	0.74	192.3
			G	0.11 (0.08)	0.65 (0.09)	143.3 (43.4)
	◑		C1	0.03	0.52	180.9
			C2	0.11	0.45	123.9
			C3	0.15	0.48	105.8
			G	0.09 (0.06)	0.49 (0.03)	136.8 (39.2)
	○		C1	0.08	0.57	154.3
			C2	0.14	0.51	116.8
			C3	0.08	0.61	149.1
			G	0.10 (0.03)	0.57 (0.05)	140.1 (20.3)
Superior Longitudinal	◐		C1	0.61	0.91	40.2
			C2	0.69	0.80	14.6
			C3	0.49	0.84	52.1
			G	0.60 (0.10)	0.85 (0.06)	35.6 (19.2)
	◑		C1	0.81	0.90	10.8
			C2	0.44	0.59	30.4
			C3	0.35	0.42	17.6
			G	0.53 (0.24)	0.64 (0.24)	19.6 (10.0)
	○		C1	0.71	0.91	25.5
			C2	0.56	0.70	22.5
			C3	0.42	0.63	34.9
			G	0.56 (0.14)	0.74 (0.14)	27.6 (6.4)
Uncinate	◐		C1	–	0.65	–
			C2	0.09	0.48	134.7
			C3	–	0.49	–
			G	0.09	0.54 (0.10)	134.7
	◑		C1	–	0.71	–
			C2	0.10	0.59	141.5
			C3	0.04	0.40	165.8
			G	0.07 (0.04)	0.57 (0.16)	153.7 (17.2)
	○		C1	–	0.68	–
			C2	0.10	0.53	138.1
			C3	0.04	0.44	165.8
			G	0.07 (0.04)	0.55 (0.12)	152.0 (19.6)

continued on next page

Table C.1: Tract Delineation (Dice) Summary — continued from previous page

Tract	Laterality	Color	ID	Dice		
				DWI	FWE	Δ (%)
Vertical Occipital	◐		C1	–	0.49	–
			C2	0.00	0.40	200.0
			C3	0.00	0.77	200.0
			G	0.00 (0.00)	0.55 (0.19)	200.0 (0.0)
	◑		C1	–	0.45	–
			C2	–	0.06	–
			C3	–	0.27	–
			G	–	0.26 (0.19)	–
	○		C1	–	0.47	–
			C2	0.00	0.23	200.0
			C3	0.00	0.52	200.0
			G	0.00 (0.00)	0.41 (0.15)	200.0 (0.0)
All Tracts			G	0.38 (0.24)	0.58 (0.17)	71.1 (58.7)

Note. Participant rows report individual values; G rows report mean (SD) for available participants. For bilateral tracts, left-hemisphere (◐), right-hemisphere (◑), and bilateral-average (○) values are reported; unilateral tracts (●) are reported as individual values. The All Tracts row reports the mean (SD) of the 14 tract-specific group means.

D Tract-Profile Reliability (ICC) — DKI-FA

Table D.1: Intraclass correlation coefficient (ICC(2,1)) for the conventional and babyFWE pipelines, with raw difference (FWE − DWI), for each participant and tract ($n = 3$; see Methods and Results, Figure 3.3), for DKI-FA.

Tract	Laterality	Color	ID	ICC		
				DWI	FWE	Δ
Anterior Thalamic	◐	●	C1	0.89	0.86	−0.03
		●	C2	0.93	0.96	0.03
		●	C3	0.66	0.92	0.26
		●	G	0.83 (0.15)	0.91 (0.05)	0.09 (0.16)
	◑	●	C1	–	0.87	–
		●	C2	0.75	0.74	−0.01
		●	C3	–	0.61	–
		●	G	0.75	0.74 (0.13)	−0.01
	○	●	C1	0.89	0.86	−0.03
		●	C2	0.84	0.85	0.01
		●	C3	0.66	0.76	0.26
		●	G	0.80 (0.12)	0.83 (0.05)	0.08 (0.16)
Arcuate	◐	●	C1	0.65	0.77	0.12
		●	C2	0.66	0.89	0.23
		●	C3	0.39	0.66	0.27
		●	G	0.56 (0.15)	0.77 (0.12)	0.21 (0.08)
	◑	●	C1	0.23	0.86	0.63
		●	C2	0.71	0.48	−0.23
		●	C3	0.60	0.40	−0.20
		●	G	0.52 (0.25)	0.58 (0.25)	0.07 (0.49)
	○	●	C1	0.44	0.81	0.37
		●	C2	0.68	0.69	0.00
		●	C3	0.50	0.53	0.03
		●	G	0.54 (0.13)	0.68 (0.14)	0.14 (0.20)

continued on next page

Table D.1: Tract Profile (ICC) Summary – DKI-FA — continued from previous page

Tract	Laterality	Color	ID	ICC		
				DWI	FWE	Δ
Cingulum Cingulate	◐	●	C1	0.69	0.76	0.07
		●	C2	0.82	0.37	−0.45
		●	C3	0.77	0.59	−0.18
		●	G	0.76 (0.06)	0.58 (0.20)	−0.19 (0.26)
	◑	●	C1	0.35	0.65	0.29
		●	C2	0.10	0.42	0.33
		●	C3	0.07	0.53	0.46
		●	G	0.17 (0.16)	0.53 (0.11)	0.36 (0.09)
	○	●	C1	0.52	0.71	0.18
		●	C2	0.46	0.40	−0.06
		●	C3	0.42	0.56	0.14
		●	G	0.47 (0.05)	0.55 (0.15)	0.09 (0.13)
Corticospinal	◐	●	C1	0.90	0.86	−0.04
		●	C2	0.90	0.55	−0.34
		●	C3	0.95	0.42	−0.53
		●	G	0.92 (0.03)	0.61 (0.23)	−0.31 (0.25)
	◑	●	C1	0.75	0.91	0.16
		●	C2	0.90	0.91	0.01
		●	C3	0.71	0.93	0.22
		●	G	0.78 (0.10)	0.91 (0.01)	0.13 (0.11)
	○	●	C1	0.82	0.88	0.06
		●	C2	0.90	0.73	−0.17
		●	C3	0.83	0.67	−0.15
		●	G	0.85 (0.04)	0.76 (0.11)	−0.09 (0.13)
Forceps Major	●	●	C1	0.98	0.66	−0.32
		●	C2	0.07	0.53	0.46
		●	C3	0.98	0.98	0.00
		●	G	0.68 (0.52)	0.72 (0.23)	0.05 (0.39)
Forceps Minor	●	●	C1	0.79	0.90	0.11
		●	C2	0.96	0.98	0.03
		●	C3	–	0.00	–
		●	G	0.87 (0.12)	0.63 (0.54)	0.07 (0.06)

continued on next page

Table D.1: Tract Profile (ICC) Summary – DKI-FA — continued from previous page

Tract	Laterality	Color	ID	ICC		
				DWI	FWE	Δ
Inferior Fronto-Occipital	◐	●	C1	–	0.75	–
		●	C2	–	0.80	–
		●	C3	–	0.88	–
		●	G	–	0.81 (0.07)	–
	◑	●	C1	–	0.76	–
		●	C2	–	0.82	–
		●	C3	–	0.23	–
		●	G	–	0.60 (0.32)	–
	○	●	C1	–	0.75	–
		●	C2	–	0.81	–
		●	C3	–	0.56	–
		●	G	–	0.71 (0.13)	–
Inferior Longitudinal	◐	●	C1	0.58	0.81	0.23
		●	C2	0.66	0.88	0.22
		●	C3	0.63	0.91	0.28
		●	G	0.63 (0.04)	0.87 (0.05)	0.24 (0.03)
	◑	●	C1	0.86	0.90	0.04
		●	C2	0.79	0.64	−0.15
		●	C3	0.63	0.81	0.18
		●	G	0.76 (0.12)	0.78 (0.13)	0.02 (0.17)
	○	●	C1	0.72	0.85	0.13
		●	C2	0.73	0.76	0.04
		●	C3	0.63	0.86	0.23
		●	G	0.69 (0.05)	0.83 (0.05)	0.13 (0.10)
Middle Longitudinal	◐	●	C1	0.72	0.79	0.07
		●	C2	0.83	0.92	0.08
		●	C3	0.81	0.94	0.13
		●	G	0.79 (0.06)	0.88 (0.08)	0.10 (0.03)
	◑	●	C1	–	0.87	–
		●	C2	0.31	0.78	0.47
		●	C3	–	0.81	–
		●	G	0.31	0.82 (0.05)	0.47
	○	●	C1	0.72	0.83	0.07
		●	C2	0.57	0.85	0.28
		●	C3	0.81	0.88	0.13
		●	G	0.70 (0.12)	0.85 (0.02)	0.16 (0.11)

continued on next page

Table D.1: Tract Profile (ICC) Summary – DKI-FA — continued from previous page

Tract	Laterality	Color	ID	ICC		
				DWI	FWE	Δ
Optic Radiation	◐	●	C1	0.73	0.95	0.23
		●	C2	0.27	0.24	−0.04
		●	C3	0.60	0.82	0.21
		●	G	0.54 (0.24)	0.67 (0.38)	0.13 (0.15)
	◑	●	C1	0.80	0.78	−0.02
		●	C2	0.23	0.88	0.64
		●	C3	0.49	0.63	0.14
		●	G	0.51 (0.28)	0.76 (0.12)	0.25 (0.35)
	○	●	C1	0.76	0.87	0.10
		●	C2	0.25	0.56	0.30
		●	C3	0.55	0.72	0.18
		●	G	0.52 (0.26)	0.72 (0.16)	0.19 (0.10)
Posterior Arcuate	◐	●	C1	0.28	0.86	0.58
		●	C2	0.53	0.73	0.20
		●	C3	0.51	0.71	0.20
		●	G	0.44 (0.14)	0.77 (0.08)	0.33 (0.22)
	◑	●	C1	−0.42	0.85	1.27
		●	C2	0.80	0.56	−0.24
		●	C3	0.44	0.85	0.40
		●	G	0.27 (0.62)	0.75 (0.17)	0.48 (0.76)
	○	●	C1	−0.07	0.86	0.92
		●	C2	0.66	0.64	−0.02
		●	C3	0.48	0.78	0.30
		●	G	0.36 (0.38)	0.76 (0.11)	0.40 (0.48)
Superior Longitudinal	◐	●	C1	0.71	0.96	0.25
		●	C2	0.90	0.95	0.06
		●	C3	0.67	0.96	0.29
		●	G	0.76 (0.12)	0.96 (0.00)	0.20 (0.13)
	◑	●	C1	0.83	0.98	0.15
		●	C2	0.77	0.88	0.11
		●	C3	0.74	0.77	0.03
		●	G	0.78 (0.05)	0.88 (0.11)	0.10 (0.06)
	○	●	C1	0.77	0.97	0.20
		●	C2	0.84	0.92	0.08
		●	C3	0.70	0.86	0.16
		●	G	0.77 (0.07)	0.92 (0.05)	0.15 (0.06)

continued on next page

Table D.1: Tract Profile (ICC) Summary – DKI-FA — continued from previous page

Tract	Laterality	Color	ID	ICC		
				DWI	FWE	Δ
Uncinate	◐	●	C1	–	0.88	–
		●	C2	0.50	0.71	0.21
		●	C3	–	0.70	–
		●	G	0.50	0.77 (0.10)	0.21
	◑	●	C1	–	0.96	–
		●	C2	0.33	0.66	0.33
		●	C3	−0.01	0.60	0.61
		●	G	0.16 (0.24)	0.74 (0.19)	0.47 (0.20)
	○	●	C1	–	0.92	–
		●	C2	0.41	0.68	0.27
		●	C3	−0.01	0.65	0.61
		●	G	0.20 (0.30)	0.75 (0.15)	0.44 (0.24)
Vertical Occipital	◐	●	C1	–	0.70	–
		●	C2	0.00	0.84	0.84
		●	C3	0.13	0.68	0.55
		●	G	0.07 (0.09)	0.74 (0.09)	0.69 (0.21)
	◑	●	C1	–	0.67	–
		●	C2	–	0.62	–
		●	C3	–	0.84	–
		●	G	–	0.71 (0.12)	–
	○	●	C1	–	0.69	–
		●	C2	0.00	0.73	0.84
		●	C3	0.13	0.76	0.55
		●	G	0.07 (0.09)	0.72 (0.04)	0.69 (0.21)
All Tracts		●	G	0.58 (0.25)	0.74 (0.09)	0.19 (0.20)

Note. Participant rows report individual values; G rows report mean (SD) for available participants. For bilateral tracts, left-hemisphere (◐), right-hemisphere (◑), and bilateral-average (○) values are reported; unilateral tracts (●) are reported as individual values. The All Tracts row reports the mean (SD) of the 14 tract-specific group means.

E Tract-Profile Reliability (ICC) — DKI-MD

Table E.1: Intraclass correlation coefficient (ICC(2,1)) for the conventional and babyFWE pipelines, with raw difference (FWE − DWI), for each participant and tract ($n = 3$; see Methods and Results, Figure 3.3), for DKI-MD.

Tract	Laterality	Color	ID	ICC		
				DWI	FWE	Δ
Anterior Thalamic	◐		C1	0.74	0.89	0.15
			C2	0.86	0.86	−0.00
			C3	−0.14	0.85	0.99
			G	0.49 (0.55)	0.86 (0.02)	0.38 (0.53)
	◑		C1	–	0.81	–
			C2	0.25	0.10	−0.16
			C3	–	0.59	–
			G	0.25	0.50 (0.37)	−0.16
	○		C1	0.74	0.85	0.15
			C2	0.56	0.48	−0.08
			C3	−0.14	0.72	0.99
			G	0.38 (0.47)	0.68 (0.19)	0.35 (0.56)
Arcuate	◐		C1	0.77	0.80	0.03
			C2	0.38	0.84	0.46
			C3	0.04	0.30	0.26
			G	0.40 (0.36)	0.65 (0.30)	0.25 (0.22)
	◑		C1	0.02	0.96	0.95
			C2	0.34	0.01	−0.33
			C3	0.01	0.38	0.37
			G	0.12 (0.19)	0.45 (0.48)	0.33 (0.64)
	○		C1	0.39	0.88	0.49
			C2	0.36	0.43	0.06
			C3	0.03	0.34	0.32
			G	0.26 (0.20)	0.55 (0.29)	0.29 (0.21)

continued on next page

Table E.1: Tract Profile (ICC) Summary – DKI-MD — continued from previous page

Tract	Laterality	Color	ID	ICC		
				DWI	FWE	Δ
Cingulum Cingulate	◐	●	C1	0.28	0.23	−0.05
		●	C2	0.12	−0.16	−0.28
		●	C3	0.65	0.40	−0.24
		●	G	0.35 (0.27)	0.16 (0.29)	−0.19 (0.13)
	◑	●	C1	0.03	0.49	0.46
		●	C2	0.59	−0.11	−0.70
		●	C3	−0.02	0.07	0.08
		●	G	0.20 (0.34)	0.15 (0.31)	−0.05 (0.59)
	○	●	C1	0.16	0.36	0.20
		●	C2	0.35	−0.13	−0.49
		●	C3	0.31	0.23	−0.08
		●	G	0.27 (0.11)	0.15 (0.26)	−0.12 (0.35)
Corticospinal	◐	●	C1	0.59	0.95	0.36
		●	C2	0.41	0.77	0.36
		●	C3	0.25	0.71	0.46
		●	G	0.42 (0.17)	0.81 (0.13)	0.39 (0.06)
	◑	●	C1	0.93	0.94	0.00
		●	C2	0.57	0.91	0.34
		●	C3	0.58	0.80	0.22
		●	G	0.69 (0.21)	0.88 (0.07)	0.19 (0.17)
	○	●	C1	0.76	0.94	0.18
		●	C2	0.49	0.84	0.35
		●	C3	0.41	0.75	0.34
		●	G	0.56 (0.18)	0.85 (0.09)	0.29 (0.09)
Forceps Major	●	●	C1	0.87	0.58	−0.29
		●	C2	−0.13	0.28	0.40
		●	C3	0.89	0.86	−0.02
		●	G	0.54 (0.58)	0.57 (0.29)	0.03 (0.35)
Forceps Minor	●	●	C1	0.49	0.84	0.34
		●	C2	0.26	0.83	0.57
		●	C3	–	−0.17	–
		●	G	0.38 (0.16)	0.50 (0.58)	0.46 (0.16)

continued on next page

Table E.1: Tract Profile (ICC) Summary – DKI-MD — continued from previous page

Tract	Laterality	Color	ID	ICC		
				DWI	FWE	Δ
Inferior Fronto-Occipital	◐	●	C1	–	0.47	–
		●	C2	–	0.64	–
		●	C3	–	0.75	–
		●	G	–	0.62 (0.14)	–
	◑	●	C1	–	0.49	–
		●	C2	–	0.27	–
		●	C3	–	0.46	–
		●	G	–	0.40 (0.12)	–
	○	●	C1	–	0.48	–
		●	C2	–	0.45	–
		●	C3	–	0.61	–
		●	G	–	0.51 (0.08)	–
Inferior Longitudinal	◐	●	C1	0.44	0.67	0.23
		●	C2	0.73	0.88	0.15
		●	C3	0.91	0.73	−0.17
		●	G	0.69 (0.24)	0.76 (0.11)	0.07 (0.22)
	◑	●	C1	0.34	0.57	0.23
		●	C2	0.71	0.70	−0.01
		●	C3	0.53	0.30	−0.22
		●	G	0.53 (0.18)	0.53 (0.20)	−0.00 (0.23)
	○	●	C1	0.39	0.62	0.23
		●	C2	0.72	0.79	0.07
		●	C3	0.72	0.52	−0.20
		●	G	0.61 (0.19)	0.64 (0.14)	0.04 (0.22)
Middle Longitudinal	◐	●	C1	0.08	0.51	0.42
		●	C2	0.70	0.55	−0.15
		●	C3	0.74	0.81	0.07
		●	G	0.51 (0.37)	0.62 (0.17)	0.12 (0.29)
	◑	●	C1	–	0.78	–
		●	C2	0.29	−0.01	−0.31
		●	C3	–	0.79	–
		●	G	0.29	0.52 (0.46)	−0.31
	○	●	C1	0.08	0.64	0.42
		●	C2	0.49	0.27	−0.23
		●	C3	0.74	0.80	0.07
		●	G	0.44 (0.33)	0.57 (0.27)	0.09 (0.32)

continued on next page

Table E.1: Tract Profile (ICC) Summary – DKI-MD — continued from previous page

Tract	Laterality	Color	ID	ICC		
				DWI	FWE	Δ
Optic Radiation	◐	●	C1	0.91	0.95	0.04
		●	C2	0.87	0.37	−0.50
		●	C3	0.95	0.82	−0.13
		●	G	0.91 (0.04)	0.71 (0.30)	−0.20 (0.27)
	◑	●	C1	0.85	0.76	−0.09
		●	C2	0.63	0.74	0.10
		●	C3	0.88	0.50	−0.38
		●	G	0.79 (0.13)	0.67 (0.15)	−0.12 (0.24)
	○	●	C1	0.88	0.86	−0.02
		●	C2	0.75	0.55	−0.20
		●	C3	0.91	0.66	−0.26
		●	G	0.85 (0.09)	0.69 (0.15)	−0.16 (0.12)
Posterior Arcuate	◐	●	C1	0.42	0.78	0.35
		●	C2	−0.08	0.20	0.28
		●	C3	0.09	0.85	0.77
		●	G	0.14 (0.26)	0.61 (0.36)	0.47 (0.26)
	◑	●	C1	−0.02	0.25	0.27
		●	C2	0.46	0.24	−0.22
		●	C3	0.09	0.40	0.32
		●	G	0.17 (0.25)	0.30 (0.09)	0.12 (0.29)
	○	●	C1	0.20	0.51	0.31
		●	C2	0.19	0.22	0.03
		●	C3	0.09	0.63	0.54
		●	G	0.16 (0.06)	0.45 (0.21)	0.29 (0.26)
Superior Longitudinal	◐	●	C1	0.27	0.95	0.68
		●	C2	0.52	0.05	−0.46
		●	C3	0.73	0.88	0.15
		●	G	0.51 (0.23)	0.63 (0.50)	0.12 (0.57)
	◑	●	C1	0.87	0.89	0.03
		●	C2	0.46	0.45	−0.01
		●	C3	−0.02	0.49	0.51
		●	G	0.43 (0.44)	0.61 (0.24)	0.17 (0.29)
	○	●	C1	0.57	0.92	0.35
		●	C2	0.49	0.25	−0.24
		●	C3	0.35	0.68	0.33
		●	G	0.47 (0.11)	0.62 (0.34)	0.15 (0.33)

continued on next page

Table E.1: Tract Profile (ICC) Summary – DKI-MD — continued from previous page

Tract	Laterality	Color	ID	ICC		
				DWI	FWE	Δ
Uncinate	◐	●	C1	–	0.84	–
		●	C2	−0.02	0.63	0.66
		●	C3	–	0.78	–
		●	G	−0.02	0.75 (0.10)	0.66
	◑	●	C1	–	0.87	–
		●	C2	0.39	0.70	0.31
		●	C3	−0.13	0.20	0.34
		●	G	0.13 (0.37)	0.59 (0.34)	0.32 (0.02)
	○	●	C1	–	0.85	–
		●	C2	0.18	0.67	0.48
		●	C3	−0.13	0.49	0.34
		●	G	0.02 (0.22)	0.67 (0.18)	0.41 (0.10)
Vertical Occipital	◐	●	C1	–	0.74	–
		●	C2	0.01	−0.05	−0.05
		●	C3	0.11	0.81	0.71
		●	G	0.06 (0.07)	0.50 (0.48)	0.33 (0.54)
	◑	●	C1	–	0.69	–
		●	C2	–	−0.02	–
		●	C3	–	0.25	–
		●	G	–	0.31 (0.36)	–
	○	●	C1	–	0.71	–
		●	C2	0.01	−0.03	−0.05
		●	C3	0.11	0.53	0.71
		●	G	0.06 (0.07)	0.40 (0.39)	0.33 (0.54)
All Tracts		●	G	0.38 (0.23)	0.56 (0.16)	0.19 (0.20)

Note. Participant rows report individual values; G rows report mean (SD) for available participants. For bilateral tracts, left-hemisphere (◐), right-hemisphere (◑), and bilateral-average (○) values are reported; unilateral tracts (●) are reported as individual values. The All Tracts row reports the mean (SD) of the 14 tract-specific group means.

F Tract-Profile Reliability (ICC) — DKI-MK

Table F.1: Intraclass correlation coefficient (ICC(2,1)) for the conventional and babyFWE pipelines, with raw difference (FWE − DWI), for each participant and tract ($n = 3$; see Methods and Results, Figure 3.3), for DKI-MK.

Tract	Laterality	Color	ID	ICC		
				DWI	FWE	Δ
Anterior Thalamic	◐	●	C1	0.40	0.57	0.17
		●	C2	0.52	0.40	−0.12
		●	C3	0.54	0.93	0.39
		●	G	0.49 (0.07)	0.64 (0.27)	0.15 (0.25)
	◑	●	C1	–	0.26	–
		●	C2	0.71	0.58	−0.13
		●	C3	–	−0.35	–
		●	G	0.71	0.16 (0.47)	−0.13
	○	●	C1	0.40	0.42	0.17
		●	C2	0.61	0.49	−0.12
		●	C3	0.54	0.29	0.39
		●	G	0.52 (0.11)	0.40 (0.10)	0.14 (0.26)
Arcuate	◐	●	C1	0.21	0.49	0.28
		●	C2	0.44	0.44	0.00
		●	C3	0.03	0.02	−0.00
		●	G	0.22 (0.21)	0.32 (0.26)	0.09 (0.16)
	◑	●	C1	0.29	0.95	0.65
		●	C2	−0.18	0.04	0.21
		●	C3	0.15	0.55	0.40
		●	G	0.09 (0.24)	0.51 (0.46)	0.42 (0.22)
	○	●	C1	0.25	0.72	0.47
		●	C2	0.13	0.24	0.11
		●	C3	0.09	0.29	0.20
		●	G	0.16 (0.08)	0.42 (0.26)	0.26 (0.19)

continued on next page

Table F.1: Tract Profile (ICC) Summary – DKI-MK — continued from previous page

Tract	Laterality	Color	ID	ICC		
				DWI	FWE	Δ
Cingulum Cingulate	◐	●	C1	0.53	0.49	−0.04
		●	C2	0.33	0.35	0.02
		●	C3	0.57	0.39	−0.18
		●	G	0.48 (0.13)	0.41 (0.07)	−0.07 (0.10)
	◑	●	C1	−0.13	−0.02	0.11
		●	C2	0.25	−0.11	−0.36
		●	C3	−0.65	0.23	0.88
		●	G	−0.18 (0.45)	0.03 (0.18)	0.21 (0.63)
	○	●	C1	0.20	0.23	0.03
		●	C2	0.29	0.12	−0.17
		●	C3	−0.04	0.31	0.35
		●	G	0.15 (0.17)	0.22 (0.09)	0.07 (0.26)
Corticospinal	◐	●	C1	0.57	0.89	0.32
		●	C2	0.77	0.84	0.07
		●	C3	0.88	0.81	−0.07
		●	G	0.74 (0.16)	0.85 (0.04)	0.11 (0.20)
	◑	●	C1	0.29	0.52	0.23
		●	C2	0.70	0.83	0.13
		●	C3	0.82	0.91	0.09
		●	G	0.60 (0.28)	0.75 (0.21)	0.15 (0.07)
	○	●	C1	0.43	0.70	0.27
		●	C2	0.73	0.83	0.10
		●	C3	0.85	0.86	0.01
		●	G	0.67 (0.22)	0.80 (0.08)	0.13 (0.13)
Forceps Major	●	●	C1	0.90	0.60	−0.30
		●	C2	−0.06	−0.05	0.01
		●	C3	0.66	0.73	0.07
		●	G	0.50 (0.50)	0.42 (0.42)	−0.07 (0.20)
Forceps Minor	●	●	C1	0.68	0.85	0.17
		●	C2	0.40	0.83	0.42
		●	C3	–	−0.06	–
		●	G	0.54 (0.19)	0.54 (0.52)	0.30 (0.18)

continued on next page

Table F.1: Tract Profile (ICC) Summary – DKI-MK — continued from previous page

Tract	Laterality	Color	ID	ICC		
				DWI	FWE	Δ
Inferior Fronto-Occipital	◐	●	C1	–	0.61	–
		●	C2	–	0.43	–
		●	C3	–	0.57	–
		●	G	–	0.54 (0.09)	–
	◑	●	C1	–	0.65	–
		●	C2	–	0.23	–
		●	C3	–	−0.04	–
		●	G	–	0.28 (0.35)	–
	○	●	C1	–	0.63	–
		●	C2	–	0.33	–
		●	C3	–	0.27	–
		●	G	–	0.41 (0.19)	–
Inferior Longitudinal	◐	●	C1	0.33	0.60	0.27
		●	C2	0.93	0.93	0.00
		●	C3	0.76	0.88	0.12
		●	G	0.67 (0.31)	0.80 (0.18)	0.13 (0.13)
	◑	●	C1	0.75	0.82	0.07
		●	C2	0.74	0.63	−0.11
		●	C3	0.55	0.06	−0.49
		●	G	0.68 (0.11)	0.50 (0.40)	−0.18 (0.29)
	○	●	C1	0.54	0.71	0.17
		●	C2	0.84	0.78	−0.06
		●	C3	0.66	0.47	−0.19
		●	G	0.68 (0.15)	0.65 (0.16)	−0.02 (0.18)
Middle Longitudinal	◐	●	C1	0.10	0.32	0.22
		●	C2	0.51	0.82	0.31
		●	C3	0.62	0.67	0.06
		●	G	0.41 (0.27)	0.60 (0.25)	0.20 (0.13)
	◑	●	C1	–	0.92	–
		●	C2	0.81	0.81	0.00
		●	C3	–	0.44	–
		●	G	0.81	0.72 (0.25)	0.00
	○	●	C1	0.10	0.62	0.22
		●	C2	0.66	0.81	0.16
		●	C3	0.62	0.56	0.06
		●	G	0.46 (0.31)	0.66 (0.13)	0.15 (0.08)

continued on next page

Table F.1: Tract Profile (ICC) Summary – DKI-MK — continued from previous page

Tract	Laterality	Color	ID	ICC		
				DWI	FWE	Δ
Optic Radiation	◐	●	C1	0.18	0.84	0.66
		●	C2	0.73	0.75	0.02
		●	C3	0.69	0.91	0.22
		●	G	0.53 (0.31)	0.83 (0.08)	0.30 (0.33)
	◑	●	C1	0.17	0.81	0.64
		●	C2	0.05	0.64	0.59
		●	C3	0.50	0.47	−0.04
		●	G	0.24 (0.23)	0.64 (0.17)	0.40 (0.37)
	○	●	C1	0.17	0.82	0.65
		●	C2	0.39	0.69	0.30
		●	C3	0.60	0.69	0.09
		●	G	0.39 (0.21)	0.74 (0.08)	0.35 (0.28)
Posterior Arcuate	◐	●	C1	−0.03	0.75	0.79
		●	C2	0.12	0.42	0.30
		●	C3	0.33	0.68	0.35
		●	G	0.14 (0.18)	0.62 (0.18)	0.48 (0.27)
	◑	●	C1	0.09	0.61	0.53
		●	C2	0.45	0.51	0.06
		●	C3	0.56	0.62	0.06
		●	G	0.37 (0.25)	0.58 (0.06)	0.21 (0.27)
	○	●	C1	0.03	0.68	0.66
		●	C2	0.29	0.47	0.18
		●	C3	0.45	0.65	0.20
		●	G	0.25 (0.21)	0.60 (0.12)	0.35 (0.27)
Superior Longitudinal	◐	●	C1	0.48	0.83	0.35
		●	C2	0.04	0.51	0.48
		●	C3	−0.27	0.55	0.82
		●	G	0.08 (0.38)	0.63 (0.18)	0.55 (0.24)
	◑	●	C1	0.74	0.82	0.08
		●	C2	0.46	0.21	−0.26
		●	C3	−0.32	0.55	0.86
		●	G	0.30 (0.55)	0.53 (0.31)	0.23 (0.57)
	○	●	C1	0.61	0.83	0.22
		●	C2	0.25	0.36	0.11
		●	C3	−0.29	0.55	0.84
		●	G	0.19 (0.46)	0.58 (0.23)	0.39 (0.40)

continued on next page

Table F.1: Tract Profile (ICC) Summary – DKI-MK — continued from previous page

Tract	Laterality	Color	ID	ICC		
				DWI	FWE	Δ
Uncinate	◐	●	C1	–	0.89	–
		●	C2	0.01	0.22	0.21
		●	C3	–	0.11	–
		●	G	0.01	0.41 (0.42)	0.21
	◑	●	C1	–	0.93	–
		●	C2	−0.24	0.74	0.97
		●	C3	0.21	0.65	0.44
		●	G	−0.01 (0.32)	0.77 (0.15)	0.71 (0.38)
	○	●	C1	–	0.91	–
		●	C2	−0.11	0.48	0.59
		●	C3	0.21	0.38	0.44
		●	G	0.05 (0.23)	0.59 (0.28)	0.52 (0.11)
Vertical Occipital	◐	●	C1	–	0.46	–
		●	C2	0.04	0.61	0.58
		●	C3	−0.12	0.49	0.61
		●	G	−0.04 (0.11)	0.52 (0.08)	0.59 (0.02)
	◑	●	C1	–	0.29	–
		●	C2	–	0.57	–
		●	C3	–	0.89	–
		●	G	–	0.58 (0.30)	–
	○	●	C1	–	0.37	–
		●	C2	0.04	0.59	0.58
		●	C3	−0.12	0.69	0.61
		●	G	−0.04 (0.11)	0.55 (0.16)	0.59 (0.02)
All Tracts		●	G	0.35 (0.24)	0.54 (0.15)	0.24 (0.20)

Note. Participant rows report individual values; G rows report mean (SD) for available participants. For bilateral tracts, left-hemisphere (◐), right-hemisphere (◑), and bilateral-average (○) values are reported; unilateral tracts (●) are reported as individual values. The All Tracts row reports the mean (SD) of the 14 tract-specific group means.

G Tract-Profile Reliability (ICC) — DKI-AWF

Table G.1: Intraclass correlation coefficient (ICC(2,1)) for the conventional and babyFWE pipelines, with raw difference (FWE − DWI), for each participant and tract ($n = 3$; see Methods and Results, Figure 3.3), for DKI-AWF.

Tract	Laterality	Color	ID	ICC		
				DWI	FWE	Δ
Anterior Thalamic	◐	●	C1	0.55	0.76	0.21
		●	C2	0.52	0.64	0.12
		●	C3	0.81	0.97	0.17
		●	G	0.62 (0.16)	0.79 (0.17)	0.16 (0.05)
	◑	●	C1	–	0.80	–
		●	C2	0.86	0.88	0.02
		●	C3	–	0.54	–
		●	G	0.86	0.74 (0.18)	0.02
	○	●	C1	0.55	0.78	0.21
		●	C2	0.69	0.76	0.07
		●	C3	0.81	0.76	0.17
		●	G	0.68 (0.13)	0.77 (0.01)	0.15 (0.07)
Arcuate	◐	●	C1	0.36	0.41	0.05
		●	C2	0.01	0.41	0.39
		●	C3	0.04	0.32	0.28
		●	G	0.14 (0.19)	0.38 (0.05)	0.24 (0.17)
	◑	●	C1	0.61	0.92	0.31
		●	C2	0.05	0.38	0.34
		●	C3	0.25	0.08	−0.17
		●	G	0.30 (0.29)	0.46 (0.42)	0.16 (0.28)
	○	●	C1	0.48	0.66	0.18
		●	C2	0.03	0.39	0.36
		●	C3	0.15	0.20	0.06
		●	G	0.22 (0.24)	0.42 (0.23)	0.20 (0.15)

continued on next page

Table G.1: Tract Profile (ICC) Summary – DKI-AWF — continued from previous page

Tract	Laterality	Color	ID	ICC		
				DWI	FWE	Δ
Cingulum Cingulate	◐	●	C1	0.51	0.54	0.03
		●	C2	0.75	0.76	0.01
		●	C3	0.40	0.68	0.27
		●	G	0.55 (0.18)	0.66 (0.11)	0.10 (0.15)
	◑	●	C1	0.48	0.62	0.14
		●	C2	0.24	0.66	0.41
		●	C3	−0.39	0.40	0.79
		●	G	0.11 (0.45)	0.56 (0.14)	0.45 (0.33)
	○	●	C1	0.49	0.58	0.08
		●	C2	0.50	0.71	0.21
		●	C3	0.01	0.54	0.53
		●	G	0.33 (0.28)	0.61 (0.09)	0.27 (0.23)
Corticospinal	◐	●	C1	0.85	0.96	0.10
		●	C2	0.81	0.79	−0.02
		●	C3	0.78	0.74	−0.03
		●	G	0.81 (0.04)	0.83 (0.11)	0.02 (0.07)
	◑	●	C1	0.56	0.59	0.04
		●	C2	0.95	0.92	−0.04
		●	C3	0.70	0.95	0.25
		●	G	0.74 (0.20)	0.82 (0.20)	0.08 (0.15)
	○	●	C1	0.71	0.77	0.07
		●	C2	0.88	0.85	−0.03
		●	C3	0.74	0.85	0.11
		●	G	0.77 (0.09)	0.83 (0.04)	0.05 (0.07)
Forceps Major	●	●	C1	0.74	0.76	0.02
		●	C2	−0.00	0.23	0.23
		●	C3	0.64	0.86	0.23
		●	G	0.46 (0.40)	0.62 (0.34)	0.16 (0.12)
Forceps Minor	●	●	C1	0.52	0.88	0.36
		●	C2	0.93	0.98	0.05
		●	C3	–	0.12	–
		●	G	0.72 (0.28)	0.66 (0.47)	0.21 (0.22)

continued on next page

Table G.1: Tract Profile (ICC) Summary – DKI-AWF — continued from previous page

Tract	Laterality	Color	ID	ICC		
				DWI	FWE	Δ
Inferior Fronto-Occipital	◐	●	C1	–	0.10	–
		●	C2	–	0.07	–
		●	C3	–	0.61	–
		●	G	–	0.26 (0.31)	–
	◑	●	C1	–	0.68	–
		●	C2	–	0.18	–
		●	C3	–	0.22	–
		●	G	–	0.36 (0.28)	–
	○	●	C1	–	0.39	–
		●	C2	–	0.12	–
		●	C3	–	0.42	–
		●	G	–	0.31 (0.16)	–
Inferior Longitudinal	◐	●	C1	0.62	0.64	0.02
		●	C2	0.88	0.93	0.05
		●	C3	0.63	0.84	0.21
		●	G	0.71 (0.15)	0.80 (0.15)	0.09 (0.10)
	◑	●	C1	0.67	0.85	0.18
		●	C2	0.66	0.63	−0.03
		●	C3	0.36	0.14	−0.21
		●	G	0.56 (0.18)	0.54 (0.36)	−0.02 (0.20)
	○	●	C1	0.64	0.74	0.10
		●	C2	0.77	0.78	0.01
		●	C3	0.49	0.49	−0.00
		●	G	0.63 (0.14)	0.67 (0.16)	0.04 (0.06)
Middle Longitudinal	◐	●	C1	0.08	0.61	0.53
		●	C2	0.61	0.89	0.28
		●	C3	0.59	0.76	0.17
		●	G	0.43 (0.30)	0.75 (0.14)	0.33 (0.19)
	◑	●	C1	–	0.83	–
		●	C2	0.93	0.86	−0.07
		●	C3	–	0.65	–
		●	G	0.93	0.78 (0.11)	−0.07
	○	●	C1	0.08	0.72	0.53
		●	C2	0.77	0.87	0.10
		●	C3	0.59	0.71	0.17
		●	G	0.48 (0.36)	0.77 (0.09)	0.27 (0.23)

continued on next page

Table G.1: Tract Profile (ICC) Summary – DKI-AWF — continued from previous page

Tract	Laterality	Color	ID	ICC		
				DWI	FWE	Δ
Optic Radiation	◐	●	C1	0.46	0.64	0.18
		●	C2	0.67	0.50	−0.17
		●	C3	0.36	0.43	0.06
		●	G	0.50 (0.15)	0.52 (0.11)	0.03 (0.18)
	◑	●	C1	0.47	0.80	0.33
		●	C2	−0.12	0.57	0.68
		●	C3	0.90	0.20	−0.69
		●	G	0.42 (0.51)	0.52 (0.30)	0.11 (0.71)
	○	●	C1	0.46	0.72	0.26
		●	C2	0.28	0.53	0.26
		●	C3	0.63	0.32	−0.32
		●	G	0.46 (0.18)	0.52 (0.20)	0.07 (0.33)
Posterior Arcuate	◐	●	C1	−0.17	0.59	0.76
		●	C2	0.72	0.68	−0.04
		●	C3	0.64	0.59	−0.06
		●	G	0.40 (0.49)	0.62 (0.05)	0.22 (0.47)
	◑	●	C1	−0.19	0.49	0.68
		●	C2	0.65	0.65	0.00
		●	C3	0.47	0.68	0.22
		●	G	0.31 (0.44)	0.61 (0.11)	0.30 (0.34)
	○	●	C1	−0.18	0.54	0.72
		●	C2	0.68	0.66	−0.02
		●	C3	0.56	0.64	0.08
		●	G	0.35 (0.46)	0.61 (0.06)	0.26 (0.40)
Superior Longitudinal	◐	●	C1	0.86	0.91	0.04
		●	C2	0.49	0.59	0.10
		●	C3	0.17	0.57	0.40
		●	G	0.51 (0.35)	0.69 (0.19)	0.18 (0.19)
	◑	●	C1	0.92	0.73	−0.19
		●	C2	0.76	0.64	−0.13
		●	C3	−0.25	0.73	0.98
		●	G	0.48 (0.63)	0.70 (0.05)	0.22 (0.66)
	○	●	C1	0.89	0.82	−0.07
		●	C2	0.63	0.61	−0.01
		●	C3	−0.04	0.65	0.69
		●	G	0.49 (0.48)	0.69 (0.11)	0.20 (0.42)

continued on next page

Table G.1: Tract Profile (ICC) Summary – DKI-AWF — continued from previous page

Tract	Laterality	Color	ID	ICC		
				DWI	FWE	Δ
Uncinate	◐	●	C1	–	0.79	–
		●	C2	0.30	0.01	−0.30
		●	C3	–	−0.19	–
		●	G	0.30	0.20 (0.52)	−0.30
	◑	●	C1	–	0.84	–
		●	C2	0.14	0.48	0.34
		●	C3	0.08	0.72	0.63
		●	G	0.11 (0.04)	0.68 (0.18)	0.49 (0.21)
	○	●	C1	–	0.81	–
		●	C2	0.22	0.24	0.02
		●	C3	0.08	0.26	0.63
		●	G	0.15 (0.10)	0.44 (0.32)	0.33 (0.43)
Vertical Occipital	◐	●	C1	–	0.27	–
		●	C2	0.15	0.60	0.45
		●	C3	−0.26	0.68	0.94
		●	G	−0.06 (0.29)	0.52 (0.22)	0.70 (0.35)
	◑	●	C1	–	0.24	–
		●	C2	–	0.66	–
		●	C3	–	0.81	–
		●	G	–	0.57 (0.29)	–
	○	●	C1	–	0.26	–
		●	C2	0.15	0.63	0.45
		●	C3	−0.26	0.75	0.94
		●	G	−0.06 (0.29)	0.54 (0.25)	0.70 (0.35)
All Tracts		●	G	0.44 (0.24)	0.60 (0.15)	0.22 (0.17)

Note. Participant rows report individual values; G rows report mean (SD) for available participants. For bilateral tracts, left-hemisphere (◐), right-hemisphere (◑), and bilateral-average (○) values are reported; unilateral tracts (●) are reported as individual values. The All Tracts row reports the mean (SD) of the 14 tract-specific group means.

H Tract Yield Summary

Table H.1: Tract yield and raw percentage-point differences (FWE − DWI) for the conventional and babyFWE pipelines, reported for each participant and tract ($n = 3$; see Methods and Results, Figure 3.4).

Tract	Laterality	Color	ID	Yield		
				DWI	FWE	Δ (%)
Anterior Thalamic	◐	●	C1	100	100	0
		●	C2	100	100	0
		●	C3	100	100	0
		●	G	100.0 (0.0)	100.0 (0.0)	0.0 (0.0)
	◑	●	C1	0	100	100
		●	C2	100	100	0
		●	C3	0	100	100
		●	G	33.3 (57.7)	100.0 (0.0)	66.7 (57.7)
	○	●	C1	50	100	50
		●	C2	100	100	0
		●	C3	50	100	50
		●	G	66.7 (28.9)	100.0 (0.0)	33.3 (28.9)
Arcuate	◐	●	C1	100	100	0
		●	C2	100	100	0
		●	C3	100	100	0
		●	G	100.0 (0.0)	100.0 (0.0)	0.0 (0.0)
	◑	●	C1	100	100	0
		●	C2	100	100	0
		●	C3	100	100	0
		●	G	100.0 (0.0)	100.0 (0.0)	0.0 (0.0)
	○	●	C1	100	100	0
		●	C2	100	100	0
		●	C3	100	100	0
		●	G	100.0 (0.0)	100.0 (0.0)	0.0 (0.0)
Cingulum Cingulate	◐	●	C1	100	100	0
		●	C2	100	100	0
		●	C3	100	100	0
		●	G	100.0 (0.0)	100.0 (0.0)	0.0 (0.0)
	◑	●	C1	100	100	0
		●	C2	100	100	0
		●	C3	100	100	0
		●	G	100.0 (0.0)	100.0 (0.0)	0.0 (0.0)
	○	●	C1	100	100	0
		●	C2	100	100	0
		●	C3	100	100	0
		●	G	100.0 (0.0)	100.0 (0.0)	0.0 (0.0)

continued on next page

Table H.1: Tract Yield Summary — continued from previous page

Tract	Laterality	Color	ID	Yield		
				DWI	FWE	Δ (%)
Corticospinal	◐	●	C1	100	100	0
		●	C2	100	100	0
		●	C3	100	100	0
		●	G	100.0 (0.0)	100.0 (0.0)	0.0 (0.0)
	◑	●	C1	100	100	0
		●	C2	100	100	0
		●	C3	100	100	0
		●	G	100.0 (0.0)	100.0 (0.0)	0.0 (0.0)
	○	●	C1	100	100	0
		●	C2	100	100	0
		●	C3	100	100	0
		●	G	100.0 (0.0)	100.0 (0.0)	0.0 (0.0)
Forceps Major	●	●	C1	100	100	0
		●	C2	100	100	0
		●	C3	100	100	0
		●	G	100.0 (0.0)	100.0 (0.0)	0.0 (0.0)
Forceps Minor	●	●	C1	100	100	0
		●	C2	100	100	0
		●	C3	0	100	100
		●	G	66.7 (57.7)	100.0 (0.0)	33.3 (57.7)
Inferior Fronto-Occipital	◐	●	C1	0	100	100
		●	C2	100	100	0
		●	C3	0	100	100
		●	G	33.3 (57.7)	100.0 (0.0)	66.7 (57.7)
	◑	●	C1	0	100	100
		●	C2	0	100	100
		●	C3	0	100	100
		●	G	0.0 (0.0)	100.0 (0.0)	100.0 (0.0)
	○	●	C1	0	100	100
		●	C2	50	100	50
		●	C3	0	100	100
		●	G	16.7 (28.9)	100.0 (0.0)	83.3 (28.9)

continued on next page

Table H.1: Tract Yield Summary — continued from previous page

Tract	Laterality	Color	ID	Yield		
				DWI	FWE	Δ (%)
Inferior Longitudinal	◐	●	C1	100	100	0
		●	C2	100	100	0
		●	C3	100	100	0
		●	G	100.0 (0.0)	100.0 (0.0)	0.0 (0.0)
	◑	●	C1	100	100	0
		●	C2	100	100	0
		●	C3	100	100	0
		●	G	100.0 (0.0)	100.0 (0.0)	0.0 (0.0)
	○	●	C1	100	100	0
		●	C2	100	100	0
		●	C3	100	100	0
		●	G	100.0 (0.0)	100.0 (0.0)	0.0 (0.0)
Middle Longitudinal	◐	●	C1	100	100	0
		●	C2	100	100	0
		●	C3	100	100	0
		●	G	100.0 (0.0)	100.0 (0.0)	0.0 (0.0)
	◑	●	C1	0	100	100
		●	C2	100	100	0
		●	C3	0	100	100
		●	G	33.3 (57.7)	100.0 (0.0)	66.7 (57.7)
	○	●	C1	50	100	50
		●	C2	100	100	0
		●	C3	50	100	50
		●	G	66.7 (28.9)	100.0 (0.0)	33.3 (28.9)
Optic Radiation	◐	●	C1	100	100	0
		●	C2	100	100	0
		●	C3	100	100	0
		●	G	100.0 (0.0)	100.0 (0.0)	0.0 (0.0)
	◑	●	C1	100	100	0
		●	C2	100	100	0
		●	C3	100	100	0
		●	G	100.0 (0.0)	100.0 (0.0)	0.0 (0.0)
	○	●	C1	100	100	0
		●	C2	100	100	0
		●	C3	100	100	0
		●	G	100.0 (0.0)	100.0 (0.0)	0.0 (0.0)

continued on next page

Table H.1: Tract Yield Summary — continued from previous page

Tract	Laterality	Color	ID	Yield		
				DWI	FWE	Δ (%)
Posterior Arcuate	◐	●	C1	0	100	100
		●	C2	0	100	100
		●	C3	0	100	100
		●	G	0.0 (0.0)	100.0 (0.0)	100.0 (0.0)
	◑	●	C1	0	100	100
		●	C2	100	100	0
		●	C3	0	100	100
		●	G	33.3 (57.7)	100.0 (0.0)	66.7 (57.7)
	○	●	C1	0	100	100
		●	C2	50	100	50
		●	C3	0	100	100
		●	G	16.7 (28.9)	100.0 (0.0)	83.3 (28.9)
Superior Longitudinal	◐	●	C1	100	100	0
		●	C2	100	100	0
		●	C3	100	100	0
		●	G	100.0 (0.0)	100.0 (0.0)	0.0 (0.0)
	◑	●	C1	100	100	0
		●	C2	100	100	0
		●	C3	100	100	0
		●	G	100.0 (0.0)	100.0 (0.0)	0.0 (0.0)
	○	●	C1	100	100	0
		●	C2	100	100	0
		●	C3	100	100	0
		●	G	100.0 (0.0)	100.0 (0.0)	0.0 (0.0)
Uncinate	◐	●	C1	0	100	100
		●	C2	100	100	0
		●	C3	0	100	100
		●	G	33.3 (57.7)	100.0 (0.0)	66.7 (57.7)
	◑	●	C1	0	100	100
		●	C2	100	100	0
		●	C3	0	100	100
		●	G	33.3 (57.7)	100.0 (0.0)	66.7 (57.7)
	○	●	C1	0	100	100
		●	C2	100	100	0
		●	C3	0	100	100
		●	G	33.3 (57.7)	100.0 (0.0)	66.7 (57.7)

continued on next page

Table H.1: Tract Yield Summary — continued from previous page

Tract	Laterality	Color	ID	Yield		
				DWI	FWE	Δ (%)
Vertical Occipital	◐	●	C1	0	100	100
		●	C2	0	100	100
		●	C3	0	100	100
		●	G	0.0 (0.0)	100.0 (0.0)	100.0 (0.0)
	◑	●	C1	0	100	100
		●	C2	0	100	100
		●	C3	0	100	100
		●	G	0.0 (0.0)	100.0 (0.0)	100.0 (0.0)
	○	●	C1	0	100	100
		●	C2	0	100	100
		●	C3	0	100	100
		●	G	0.0 (0.0)	100.0 (0.0)	100.0 (0.0)
All Tracts		●	G	69.0 (37.5)	100.0 (0.0)	31.0 (37.5)

Note. Participant rows report individual values; G rows report mean (SD) for available participants. For bilateral tracts, left-hemisphere (◐), right-hemisphere (◑), and bilateral-average (○) values are reported; unilateral tracts (●) are reported as individual values. The All Tracts row reports the mean (SD) of the 14 tract-specific group means.